Interacting Rydberg and valence states in radicals and molecules: experimental and theoretical studies

Hanna Reisler [a]; Anna I. Krylov [a]

[a] Department of Chemistry, University of Southern California, Los Angeles, CA 90089-0482, USA

PLEASE SCROLL DOWN FOR ARTICLE

Taylor & Francis
Taylor & Francis Group

REVIEW ARTICLE

Interacting Rydberg and valence states in radicals and molecules: experimental and theoretical studies

Hanna Reisler* and Anna I. Krylov*

Department of Chemistry, University of Southern California, Los Angeles, CA 90089-0482, USA

This review discusses low-lying ($n = 3$) Rydberg electronic states of molecules and radicals, in particular those that result in mixed configurations and participate in non-adiabatic interactions. Rydberg-valence interactions are ubiquitous in molecules and radicals and have important effects on potential energy surface shapes, spectroscopy, and dissociation dynamics. The review emphasises selected properties that are affected by these interactions and illustrates them with several examples, mostly involving free radicals, in which collaboration between experimental and theoretical investigations has been crucial for understanding. Specifically, the cases of substituted methyl, vinyl, and hydroxyalkyl radicals are described, as well as Rydberg states of diazomethane and the ethyl radical. The issue of triple conical intersections is also briefly discussed.

Keywords: Rydberg states; excited states; conical intersections; photodissociation; vibronic interactions; electronic structure

Contents

*Corresponding authors. Email: reisler@usc.edu; krylov@usc.edu

1. Introduction

This review discusses low-lying ($n = 3$) Rydberg electronic states of molecules and radicals, in particular those that result in mixed configurations and non-adiabatic interactions. Rydberg–valence interactions are ubiquitous in both closed-shell molecules and radicals [1–6] and have important effects on potential energy surface (PES) shapes, spectroscopy and dynamics. Many of these states are dissociative, and consequently their dynamics is intimately linked to their electronic structure. Despite their weak bonding and predissociative nature, such states are important in environments ranging from the atmosphere to the condensed phase. For example, they play a major role in electron transfer dissociation processes which are employed in mass spectrometry [7], as well as in reactions and decompositions of free radicals in excited states and weakly covalently bound dimers [5,8]. From a fundamental perspective, Rydberg–valence interactions exemplify a more general phenomenon, namely, mixing between states of different character, e.g. mixing of $\pi^* \leftarrow n$ and $\pi^* \leftarrow \pi$ configurations in nuclear bases at deformed geometries, interplay between covalent, zwitterionic states, etc.

1.1. *Molecular Rydberg states: what are they?*

Rydberg states in atoms are defined as electronically excited states derived by exciting one of the electrons into an orbital with a principal quantum number larger than that of the valence shell [9]. Because of the diffuse character of the target orbital, these states resemble the states of a hydrogen-like atom, and their energy levels behave similarly to hydrogen-like atomic levels. This is the essence of the Rydberg formula [10] that describes the convergence of the Rydberg series in many-electron atoms to the respective ionisation energies (IEs):

$$E_{\text{ex}} = IE - \frac{Ryd}{(n - \delta)^2}, \tag{1}$$

where E_{ex} is the excitation energy of the Rydberg state (in eV), $Ryd = 13.61$ eV, n is the principal quantum number and δ is the quantum defect parameter accounting for the penetration of the excited Rydberg electron to the cation core.

The distinction between Rydberg and valence states in polyatomic molecules is more qualitative. Molecular Rydberg states are excited states whose configurational expansion is dominated by configurations in which the excited electrons occupy diffuse (Rydberg) orbitals. Similar to atomic Rydberg states, molecular Rydberg states can be described as an ionised core with a weakly bound electron. Although the core is no longer spherically symmetric, the Rydberg formula can still be employed to describe energy levels. The quantum defect δ, which depends on the size and the shape of the molecule, reflects interactions with the molecular ion core and usually has values of 0.9–1.2 for s-states, 0.3–0.9 for p-states, and smaller or equal to 0.1 for d-states [10]. These ranges are much narrower within a homologous series of molecules or radicals, as will be discussed further. The situation can be more complex in molecules with closely-lying ion states due to, for example, more than one Rydberg center. In CH_3NH_2 two Rydberg series are observed, one centered on the carbon atom and the other on the nitrogen [11]. Likewise, in vinyl radicals, one Rydberg series is obtained by exciting the unpaired electron to a Rydberg state, whereas another involves similar excitation of the π bond [12].

In spite of these complications, the Rydberg formula can be used as one of the assignment criteria of electronically excited states of molecules and radicals. For example, if the quantum defect computed by using Equation (1) with known IE and E_{ex} falls within the δ interval typical of a specific class of molecules, the state with energy E_{ex} can be defined as Rydberg (provided, of course, that the character of the target MO is consistent with the suggested n, l_m quantum numbers). Larger deviations of δ from the characteristic values indicate interactions with nearby valence states and/or strong perturbations by the core. Rydberg–valence state interactions are expected to transpire in the region closest to the core, affecting vibrational levels as well.

Because the molecular core is no longer symmetric, assigning s, p or d character to a molecular Rydberg state is only qualitative, and Rydberg states with different l but with the same symmetry can interact with each other. Nevertheless, visual inspection of MOs and wave function amplitudes shows that many molecular Rydberg states can indeed be described as s, p or d states. Figure 1 shows Dyson orbitals [13] corresponding to the excited states of the NO dimer.[1] The orbitals are no longer atom-centered, and the three p-orbitals are not degenerate due to the core's asymmetry. However, because the spatial extent of the orbitals is very large relative to the dimer core, they preserve their hydrogen-atom like appearance. For example, one of the A_1 states can be easily identified as an s-like Rydberg state, whereas another A_1 and two B_2 states resemble p orbitals. Note that the spatial extent of the second B_2 state is less than that of the A_1 states, because of its interaction with a valence state of the same symmetry.

We also note the difference in size between low-lying Rydberg and valence states, which can be quantified by the expectation values of $\hat{r}^2$. $\langle r^2 \rangle$ values for valence states that involve n, π^* or σ^* are very similar to the ground state value. The difference between the $\langle r^2 \rangle$ values for ground and excited states, $\Delta \langle r^2 \rangle$, provides an even better measure of the extent of electronic density in the excited states. Because $\langle r^2 \rangle$ depends on molecular size whereas $\Delta \langle r^2 \rangle$ does not, $\Delta \langle r^2 \rangle$ enables comparisons between molecules of different sizes. In small molecules, the typical $\Delta \langle r^2 \rangle$ upon excitation from the ground to a valence state is
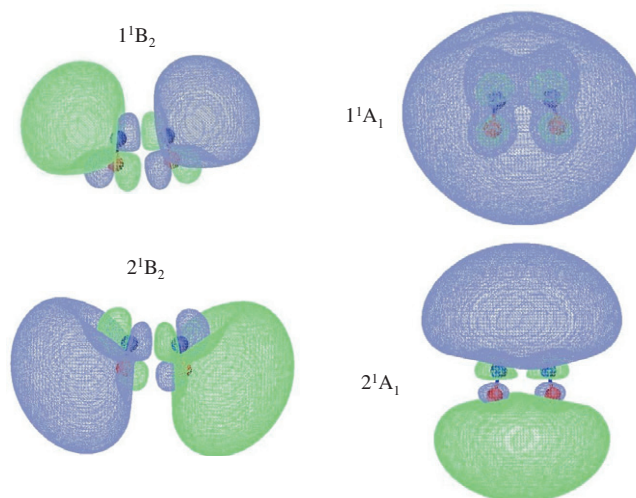
Figure 1. Dyson orbitals corresponding to the two B_2 (left) and two A_1 states of $(NO)_2$. (Note: the numbering of the states is not spectroscopic and is only used to distinguish between the states, e.g. $1A_1$ state is not the lowest A_1 state of the dimer; rather, it is the lowest of the two A_1 Rydberg states considered in this example). The B_2 states are of mixed Rydberg–valence character, whereas the A_1 states are predominantly Rydberg. Note the similarity between the respective Dyson MOs and the hydrogen-atom like orbitals.

less than 1 $(\text{Å})^2$, whereas for the 3s and 3p Rydberg state $\Delta \langle r^2 \rangle \approx 12$ $(\text{Å})^2$. This can serve as a basis for identification and assignment of Rydberg states (Section 1.2).

1.2. *Rydberg and valence states of open-shell species*

Two factors make the behaviour of excited states of open-shell systems even more complex than their closed-shell counterparts. First, the existence of a half-filled orbital affords more opportunities for excitation, namely, promotion of an unpaired electron to an empty orbital and promotion of an electron from a doubly occupied orbital to the half-filled orbital. This increases the density of electronic states and the opportunities for couplings. Second, the IEs of many organic radicals and molecules are lower than 9.0 eV [14]. According to the Rydberg formula [10], in these cases excitation to their lowest Rydberg s state would lie at < 5.5 eV or at wavelengths > 200 nm, where many strong valence (e.g. $\pi\pi^*$) or charge transfer transitions lie. In addition, the lowest energy Rydberg states, which interact most strongly with the valence states, often have quantum defects larger than predicted by the Rydberg formula, lowering their energy even further. Most hydrocarbon free radicals have IE < 9 eV and, because of hyperconjugation [11,15–20], the IEs of many organic closed-shell molecules decrease rapidly with increasing size of the hydrocarbon chain and can be as low as those of radicals. Therefore, the effects described in this review are manifest in the excited state behaviour of a large number of molecules.

The outcome is that in low IE and open-shell species, valence, Rydberg and charge transfer states interact strongly in a way that profoundly influences reaction pathways.

Therefore intuition gained from studies of closed-shell molecules is often useless. Take, for example, the series of substituted methyl radicals: CH_3, CH_2F, CH_2Cl and CH_2OH (to be described in more detail further) [21–25]. Despite their similarity, each gives rise to different excited states, optical transitions and dissociation mechanisms. In CH_2Cl specific orbital overlap confers partial double-bond π character to the C–Cl bond, resulting in strongly absorbing valence bands, as opposed to strong transitions to Rydberg states in CH_2F [21]. Moreover, the valence and Rydberg orbitals in CH_2Cl are mixed in a way that depends sensitively on molecular geometry [26]. In CH_2OH, on the other hand, multiple conical intersections couple the Rydberg states to the ground state in two simultaneous dissociative coordinates [22–25].

In addition, the order of Rydberg and valence states can change within a homologous series. For example, valence states that are based on promotion of an electron in a common chromophore can remain rather constant within a homologous series, whereas the energies of the Rydberg states decrease for higher members of the series because effects such as hyperconjugation cause a decrease in IE. This, in turn, will cause a change in Rydberg–valence interactions within the series. The series of vinyl radicals described below is a good example of this effect [12]. Conversely, if the changes in IE within a homologous series are small, then the energies of the Rydberg states would be similar and substitutions may change the valence states, as was observed in the $CH_3 \rightarrow CH_2F \rightarrow CH_2Cl$ series [21].

Because open-shell systems are active players in many environments [27], it is important to develop a comprehensive understanding of their electronic interactions and dissociation at the same level already achieved for photodissociation of stable molecules [28,29].

1.3. *Signatures of Rydberg–valence interactions*

The proximity of Rydberg states to valence and charge transfer states can be manifest in many properties. For example: (i) State interactions can give rise to PESs with weakly bound or flat, shelf-like regions or multiple minima along the dissociation coordinate [30]; (ii) Avoided crossings may render the electronic nature and transition dipole moment of adiabatic dissociative states strongly dependent on nuclear geometry and (iii) The photodissociation dynamics near conical intersections and non-adiabatic transitions will be strongly influenced by the velocity and direction of traversing the intersection seam region [31–33].

The study of molecules and radicals with close-lying Rydberg and valence states poses challenges for both experiment and theory. However, when sophisticated theoretical models are combined with state-of-the-art experimental techniques, the evolution from the excited state to final products can be followed in detail, and time-resolved transformations of orbitals, couplings between electronic states and energy disposal in final products can be revealed. Recently, such cooperation between theory and experiment has led to significant advances in interpretations of experimental observations, physical explanations of observed phenomena and formulations of propensity rules.

Experimentally, with molecules composed of second row atoms, out-of-plane 3p Rydberg states and most 3d states usually live longer than a few hundred femtoseconds and are amenable to ionisation with intense nanosecond lasers. Shorter lived states can, of course, be ionised with femtosecond lasers. Rydberg states can interact with other Rydberg and valence states, including the ground state, and these couplings will be imprinted in their

photoelectron energy and angular distributions. For example, an out-of-plane vibration may induce couplings between states of different symmetry. These couplings will be encoded in the photoelectron spectra of a nominally Rydberg state and show up as new vibrational spectral features of the cation, in addition to the diagonal transitions favoured in pure Rydberg states [34–36]. By using techniques such as velocity map imaging (VMI, see further) [30,37,38], kinetic energy and angular distributions are obtained straightforwardly with resolution that is sufficient to resolve low-frequency vibrations and, in favourable cases, rotational levels [39,40].

Describing interacting states of different character is considered a difficult problem for electronic structure methodology. Indeed, a small imbalance in describing two close-lying interacting states can dramatically affect the shape of their PESs as well as their electronic properties (transition dipoles and couplings). For example, vibronic interactions [41,42] result in stiffening of the PES of the upper state, and softening of that of the lower leading to significant changes in vibrational frequencies and even lower-symmetry structures (see Figure 1 from Ref. [42]), as well as singularities (first order poles) in force constants (e.g. Figure 3 from Ref. [41]). Thus, small errors in state energies resulting in different state ordering will manifest themselves in very different PES shapes of the two states (see, e.g. [43]). Moreover, PESs and the resulting force constants are very sensitive to changes in state character upon nuclear displacements [44–46], factors that also give rise to non-adiabatic couplings and vibronic interactions.

The equation-of-motion coupled-cluster (EOM-CC) approach [47–53] is a powerful and versatile electronic structure tool capable of accurate description of multiple interacting states of different nature [53]. It describes target states as excitations from the reference state coupled-cluster wave function Ψ_{ref}:

$$\Psi = \hat{R}\Psi_{ref} = \hat{R}e^T\Phi_0 \tag{2}$$

where the operators R and T are excitation operators with respect to the reference Φ_0 (more on this below). The EOM amplitudes are found by diagonalisation of the similarity transformed Hamiltonian. Linear parameterisation of the EOM-CC wave functions and simultaneous inclusion of dynamical and non-dynamical correlation ensure flexible, balanced and accurate description of the target states. Moreover, the multistate nature of EOM-CC greatly simplifies calculations of properties relevant to state interactions, i.e. couplings, state crossings and transition dipole moments. This is an excellent method to describe accurately close-lying Rydberg and valence states.

Alternatively, correlated multiconfigurational wave functions can be computed using multi-reference approaches [54], in which each state of interest is described by a tailored multi-configurational self-consistent field (MCSCF) wave function further augmented by perturbation theory or configuration interaction to account for dynamical correlation [54].

Parallel efforts have been directed towards a theoretical understanding of non-adiabatic transitions and conical intersections [32,33,55–60]. A physical picture is now associated with concepts such as 'branching space', 'vertical and tilted cones' and the so called 'g and h vectors', which contain information on nuclear motions that result in surface degeneracies and enhanced coupling matrix elements.

It is impossible to give a comprehensive review of the vast amount of information available on the many molecular systems that involve Rydberg–valence interactions, and

therefore we have decided to emphasise in this review selected properties that are affected by these interactions and that we have encountered in our recent work. We have chosen several illustrative examples of general concepts, mostly involving free radicals, and we add our personal perspective on specific issues and trends.

The review is organised as follows. In Sections 2 and 3, we describe briefly the main theoretical and experimental methods exploited in the studies highlighted here. In Section 4, we give examples of electronic states of diazomethane that exhibit signatures of Rydberg–valence interactions, and of CH_2Cl, which displays changes in valence and Rydberg compositions along the dissociative coordinate. We also describe how the order of valence and Rydberg states changes within the homologous series of substituted vinyl and methyl radicals and discuss what affects such ordering. Section 5 describes two manifestations of Rydberg–ion core interactions. In the vinyl radical family quantum defects change within the series, whereas in diazomethane, variations in vibrational frequencies in Rydberg states reflect interactions between the Rydberg electron and the ion core. In Section 6, we give two examples of dynamics initiated on Rydberg states of free radicals that involve conical intersections, e.g. Rydberg–Rydberg and Rydberg–ground state couplings. The photodissociation of the hydroxyalkyl and ethyl radicals demonstrates how the cooperation between experiment and theory reveals specific state interactions, as well as the importance of gradients near conical intersections in controlling nuclear dynamics and branching ratios. We also touch on the issue of triple conical intersections. We end this review with some conclusions, open questions and future directions.

2. Theoretical methods: EOM-CC methods for interacting states of different nature

Although the original applications of the EOM formalism were concerned mostly with accurate energy difference calculations, i.e. excitation and IEs, the full potential of EOM as a tool for interacting electronic states of different nature has only been exploited more recently [13,61–68].

Conceptually, EOM is similar to configuration interaction (CI): target EOM states are found by diagonalising the so-called similarity transformed Hamiltonian $\overline{H} \equiv e^{-T}He^{T}$:

$$\overline{H}R = ER, \tag{3}$$

where T and R are general excitation operators w.r.t. the reference determinant $|\Phi_0\rangle$, and the amplitudes T satisfy the CC equations for the reference state $|\Phi_0\rangle$:

$$\langle \Phi_\mu | \overline{H} | \Phi_0 \rangle, \tag{4}$$

where Φ_μ denotes μ-tuply excited determinants, e.g. $\{\Phi_i^a, \Phi_{ij}^{ab}\}$ in the case of CCSD.

When $\overline{H}$ is diagonalised in the complete many-electron basis, EOM is identical to the full CI; however, in the more practical case of a truncated basis (e.g. when T and R are truncated at single and double excitations), the EOM models are numerically superior to the corresponding CI models [69] because correlation effects are 'folded in' in the transformed Hamiltonian (and because EOM is rigorously size-intensive). The computational scaling, however, is the same (e.g. both EOM-CCSD and CISD scale as N^6).

The accuracy of EOM-CCSD can be systematically improved (up to the exact FCI results) by including higher excitations explicitly or perturbatively.

What makes the EOM methods particularly attractive for studying multiple interacting states is that EOM is a *multi-state* scheme, i.e. several target states are obtained in a single diagonalisation step. This results in an improved accuracy due to built-in error cancellation and greatly simplifies the calculation of coupling elements (e.g. non-adiabatic and spin-orbit couplings) between the states. The simpler formalism also facilitates implementation of analytic gradients and properties calculations [50,70–73].

By combining different types of excitation operators and references $|\Phi_0\rangle$, different groups of target states can be accessed (see Figure 3 from [74]). For example, electronically excited states can be described when the reference $|\Phi_0\rangle$ corresponds to the ground state wavefunction, and the operators R conserve the number of electrons and total spin [49,50,75]. In the ionised/electron attached EOM models [71,73,76,77], the operators R are not electron conserving (i.e. include different number of creation and annihilation operators). These models can accurately treat ground and excited states of doublet radicals and some other open-shell systems. For example, singly ionised EOM methods, i.e. EOM-IP-CCSD and EOM-EA-CCSD, have proven useful for doublet radicals whose theoretical treatment is often plagued by symmetry breaking. Finally, the EOM-SF method [52,74,78] in which the excitation operators include spin-flip allows one to access diradicals, triradicals, problematic open-shell doublet states and bond breaking.

The CI-like form of the EOM excitation operator enables access to multi-configurational open-shell wave-functions, exactly and nearly degenerate states (e.g. Jahn-Teller pairs), as well as interacting states of different character (i.e. Rydberg and valence states). Moreover, since no assumptions on the nature of the excited states are built into the EOM-CC scheme, the varying degree of Rydberg–valence mixing is accurately reproduced (see Figure 1 from [53]).

Most of the calculations discussed in this review were performed by the EOM-EE method employing closed or open-shell reference corresponding to the ground-state wave function. In this case, the EOM operators are of $hp, 2h2p, \ldots$ (hp stands for hole-particle) type and conserve the number of α and β electrons:

$$R^{EE} = \sum_{ia} r_i^a a^+ i + \frac{1}{4} \sum_{ijab} r_{ij}^{ab} a^+ b^+ ji + \cdots, \tag{5}$$

where only $M_s = 0$ strings of creation and annihilation operators are retained yielding, for example, $\alpha \to \alpha$ and $\beta \to \beta$ excitations. Moreover, in the case of restricted references, the operators R can be trivially spin-adapted to form either singlet or triplet excitations, which generate properly spin-adapted singlet and $M_s = 0$ triplet states. However, in the case of open-shell references (e.g. doublets), the resulting states would not be spin-adapted [79]. The conservative estimate of EOM-EE-CCSD error bars for excitation energies is 0.1–0.3 eV accuracy [80], while relative spacings of excited states are usually reproduced more accurately.

In the case of open-shell, e.g. doublet references, one should be aware that different types of excited states are described with different accuracy (see Figure 3 Ref. [53]). For example, the transitions unique to radicals, i.e. those involving half-filled orbitals, form a spin-complete set. Thus, EOM-EE describes these states with accuracy similar to that of closed-shell applications, provided there is no strong spin-contamination in the reference.

The set of determinants that involves other transitions, e.g. $\pi^* \leftarrow \pi$ and $Ry \leftarrow \pi$ in vinyl, is not spin-complete, and the missing configurations appear as double excitations [81]. Since doubles are present in EOM-EE-CCSD, the EOM description of these states is not as disastrous as CIS [82], however, it is still lacking [81]. Fortunately, these states are often higher in energy than the first group. In the vinyl and related family of unsaturated hydrocarbon radicals, however, such states are important, and we have employed EOM-SF using a high-spin quartet reference to improve their description [12].

Finally, IEs required for the Rydberg formula were computed using EOM-IP-CCSD. Most of the electronic structure calculations in our groups were conducted using the *Q-CHEM* [83] and ACES II [84] electronic structure packages.

3. Experimental techniques

Although there are many different techniques to study spectroscopy and photodissociation, most of the work described in this review exploits either photoion and photoelectron imaging or time-of-flight (TOF) spectroscopies. The velocity map imaging (VMI) technique [30,37,38,85–90] now routinely achieves a resolution of $\Delta E/E \sim 2\%$ or better, which is sufficient for many applications. For higher resolution, the high-n Rydberg TOF technique is the method of choice, but it is best suited for studies of hydrogen photofragments.

Most of the features of the imaging technique have been described in a book [38] and a recent review [88], and only a brief description is given here. In VMI [87], a state-selected product is ionised by a polarised laser photon and the extracted ion cloud expands while travelling in a field-free region towards a position sensitive detector. By reversing the extraction voltage polarity, photoelectrons can be detected as well. What is special about this technique is that the electrostatic lens system is optimised such that ions of the same velocity reach the same position on the detector whatever their positions in the overlap region of the dissociation (pump) and detection/ionisation (probe) lasers are [87–90]. The expanded charged particle cloud creates a two-dimensional (2D) projection on the detector, which contains all the essential information on the velocity distribution of the selected product.

When the images possess cylindrical symmetry around the polarisation vector of the dissociation laser, which lies parallel to the detector plane, it is possible to invert the 2D image to a 3D velocity distribution, and in our work we use the Basis Set Expansion (BASEX) method [91]. Any cut through the centre graphically displays the velocity (momentum) of the particle (which is proportional to the distance from the centre of the image) and the angular distribution [38]. The angular distribution is described for one-photon excitation by the formula:

$$I(\theta) = c[1 + \beta P_2(\cos\theta)] \qquad (6)$$

where θ is the angle between the charged particle velocity vector and the laser polarisation direction, $I(\theta)$ is the intensity at angle θ, $P_2(\cos\theta)$ is the second Legendre polynomial, β is the recoil anisotropy parameter and c is a constant. In multiphoton processes, higher order $\beta_n P_n(\cos\theta)$ terms must be included and, for the polarisation conditions employed here, n is even [37,38]. The charged particle detector is coupled to a phosphor screen, and the emitted light is detected by a CCD camera.

The imaging arrangement can be used to probe other properties of the dissociation in addition to velocity (or kinetic energy) and angular distributions. These include: (i) Photofragment spectroscopy, achieved by monitoring the total charged particle signal from a state-selected fragment as a function of excitation wavelength [37,38] and (ii) Time-resolved photoion or photoelectron spectroscopy, in which the time evolution of a product is mapped by varying the delay between the pump and probe lasers, usually in the 100–3000 fs range typical of many dissociation processes and non-adiabatic transitions between electronic states [30,85].

The second method employed in the experiments described here is the core-sampling TOF technique. In brief, the core-sampling arrangement consists of a two-stage ion acceleration region, a field-free drift region and a 4-mm diameter aperture installed in front of a microchannel plate ion detector. The ion detector is positioned parallel to the plane defined by the molecular and laser beams at the end of the field-free drift region. Core sampling utilises a spatial restriction in the ion detection to eliminate contributions from off-axis ions, thereby yielding the speed distribution of the recoiling fragments in a straightforward manner, provided the speed of the fragment is not too small [92,93]

The third important method is the high-n Rydberg TOF (HRTOF) technique [94], which has been extensively used for H/D photofragment translational spectroscopy. In this technique, H or D photofragments produced in photodissociation are excited to a long-lived high-n Rydberg state via two-photon $1 + 1'$ excitation (Lyman $\alpha + $ UV). The metastable Rydberg atoms are allowed to drift in a collision-free region until they reach the detector where they are field ionised and monitored. In this method broadening due to interactions among charged particles (space charge effects) are avoided and the highest resolution is achieved. The method has been used with both molecules and radicals [94–97].

4. Rydberg–valence electronic states

4.1. *Diazomethane: Rydberg–valence interactions*

Diazomethane (CH_2N_2) is an important source of methylene and its photochemistry is relevant to the chemistry in atmospheres rich in N_2 and methane, such as in Titan, Triton and Pluto [98]. Not surprisingly, elucidating its excitation and fragmentation mechanisms has attracted interest since 1933 [99]. However, only recently have its Rydberg electronic states in the region 6.3–7.3 eV been characterised with a combination of electronic structure calculations and REMPI and photoelectron spectroscopies in a molecular beam [100,101].

In all cases where comparisons with experimental results were available [100–105], the agreement between theory and experiment was good allowing full analyses of trends in structure and vibrational frequencies while going from the neutral species to the excited Rydberg states, 2^1A_2 ($3p_y$) and 2^1B_1 ($3p_z$), and the cation. Figure 2 shows the relevant MOs of diazomethane [100]. CH_2N_2 lies in the yz plane with the z axis coinciding with the C_2 symmetry axis (CNN bond).

The lowest valence excitation promotes an electron from the π orbital to the π^* or π_σ^* orbital [106]. Because the IE of diazomethane is only 9.00 eV, the 3s, 3p and 3d Rydberg states are located in the same region as the valence states [100]. Thus, the low-lying
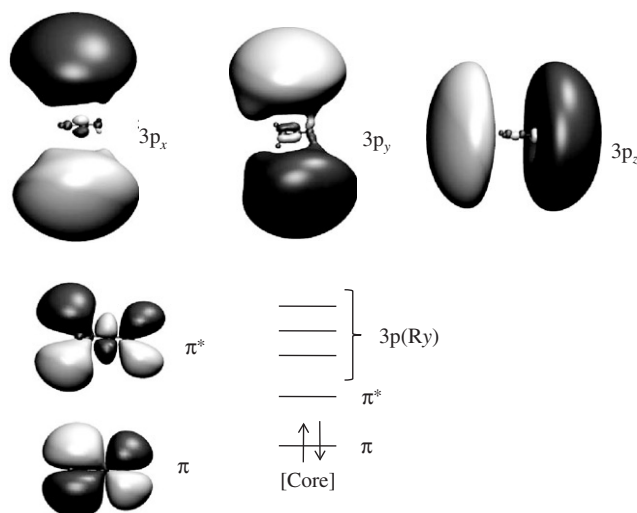
Figure 2. MOs of diazomethane. Low-lying states are derived by excitations from the HOMO to the valence π^*-like orbital and three diffuse 3p-like orbitals. The lowest valence state derived from excitation to the π_σ^* orbital does not interact with the Rydberg states and is not shown.

electronic states [100,106,107] are derived by excitations from the HOMO, which is of bonding π_{CN} character, to the corresponding π_σ^*, π^* and the three 3p Rydberg-type orbitals (Note that the open-shell character of the singlet excited states is easily described by the EOM-EE ansatz).

In the examined 6.3–7.3 eV region, three Rydberg states of 3p character contribute to the transitions, $2\,^1A_2$ ($3p_y \leftarrow \pi$), $2\,^1B_1$ ($3p_z \leftarrow \pi$), and $3\,^1A_1$ ($3p_x \leftarrow \pi$). The former two states are of mostly pure Rydberg character, as found from the EOM amplitudes and spatial extents of their wave functions. Surprisingly, the $3\,^1A_1$ state, whose $3p_x$ orbital is perpendicular to the molecular plane (Figure 2) and therefore should be the least perturbed by the cation core, is fast dissociative, as evidenced by the broad peaks observed in the REMPI spectra [100].

The calculations show that the $2\,^1A_2$ and $2\,^1B_1$ states have geometries rather similar to the cation, which has C_{2v} symmetry, with small differences due to the interactions of the electron in the 3p orbital with the nuclei charge distributions, as described in Section 5.2.

In contrast, the $3\,^1A_1$ state has a mixed Rydberg–valence character, being mixed with the $2\,^1A_1$ ($\pi^* \leftarrow \pi$) valence state.[2] The lower state, $2A_1$, is predominantly valence and repulsive, while the upper one is dominated by $3p_x \leftarrow \pi$ excitation. The strong interaction between the two states, which are more than 1 eV apart, has important consequences. For example, the $3\,^1A_1$ ($3p_x$) state borrows intensity from the valence state, making it the strongest absorbing Rydberg state. Moreover, its equilibrium geometry and vibrational frequencies strongly deviate from those of the cation and the other two Rydberg states, and it has an in-plane bent geometry of C_s symmetry. The different geometries of the $3\,^1A_1$ ($3p_x$) and the cation $1\,^2B_1$ states should give rise to a propensity for ionisation via off-diagonal transitions, resulting in multiple peaks in the photoelectron spectrum, as indeed observed in the experiment [100].
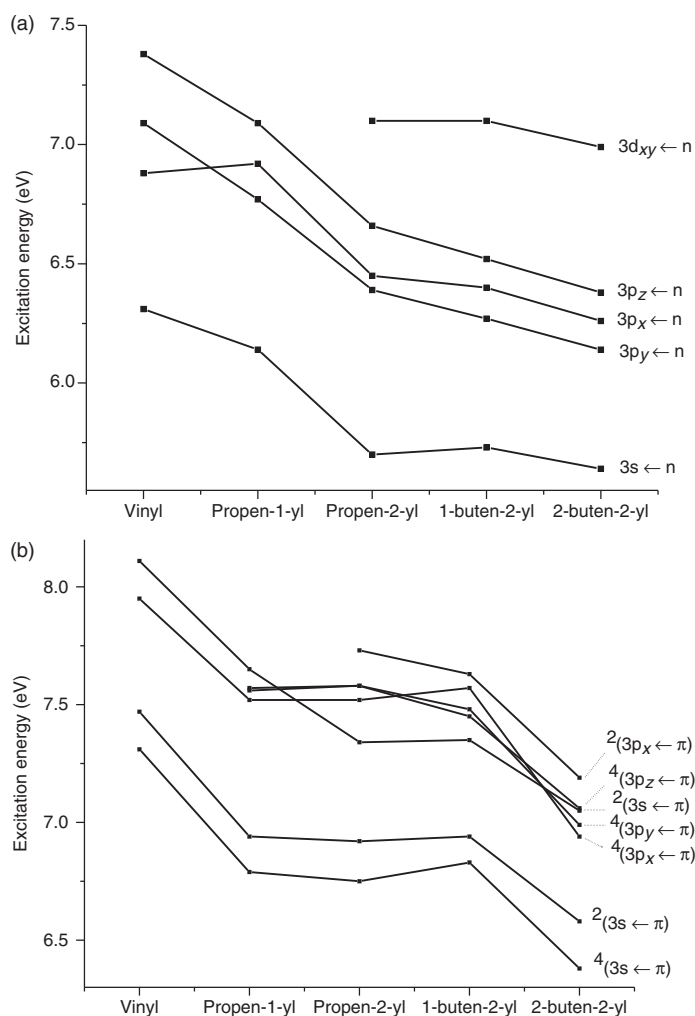
Figure 3. Changes in the $nl_m \leftarrow n$ (upper panel) and $nl_m \leftarrow \pi$ vertical excitation energies in vinyl and substituted vinyl radicals. Reprinted with permission from [12]. Copyright (2006), American Chemical Society.

4.2. *Vinyl radicals: trends in order of Rydberg and valence states*

Unsaturated hydrocarbon radicals have attracted attention as reactive intermediates in hydrocarbon combustion since the late 1960s [108–110]. Species containing the vinyl moiety are also versatile reagents in radical synthetic chemistry [111].

Low-lying valence states in a series of substituted vinyl radicals include $n \leftarrow \pi$ (the lowest electronic state of vinyl), $\pi^* \leftarrow n$, and two $\pi^* \leftarrow \pi$ states (one of these is similar to the $\pi\pi^*$ state in ethylene). However, the electronic spectra of vinyl, and even more so of the substituted radicals, are dominated by two manifolds of Rydberg states (see Figures 3–8 from [12]). One manifold is derived from excitations of the unpaired electron, whereas the second is similar to the Rydberg manifold in ethylene and is derived from

excitations of a π electron. The respective vertical IEs in vinyl are within 1 eV from each other and equal 9.63 and 10.53 eV (calculated, see [12]). Thus, it is not surprising that the two manifolds are overlapping and can interact with each other.

The relevant valence MOs (n, π and π^*) are very similar in all the substituted radicals studied in [12] (propen-1-yl, propen-2-yl, 1-buten-2-yl, and *trans*-2-buten-2-yl). Consequently, the valence excited states have similar energies in all the radicals; the changes in excitation energies are less than 0.3 eV (see Figures 8 and 10 from [12]).

The Rydberg states, however, show completely different behaviour, consistent with the Rydberg formula prediction. As the size of the radicals increases, the IEs decrease (the quantum defects, however, are not constant in the series, see Section 5.1). The calculated vertical IEs corresponding to ionisation of the unpaired electron in vinyl, propen-1-yl, propen-2-yl, 1-buten-2-yl and *trans*-2-buten-2-yl radicals are 9.63 eV, 9.28 eV, 8.79 eV, 8.66 eV and 8.51 eV, respectively. The spectral density of the $nl_m \leftarrow n$ Rydberg states increases rapidly with the decrease in IE (see Figures 3–7 from [12]). Moreover, the density of Rydberg states in the radicals is even larger due to Rydberg excitations from the π bonding orbital, which appear at relatively low energies. The IEs for ionisation from the π orbital (resulting in the triplet cation state) of vinyl, propen-1-yl, and propen-2-yl are 10.53 eV, 9.78 eV and 9.76 eV, respectively. The energies of the Rydberg states in both manifolds follow the trend in IE, in agreement with Equation (1). This is shown in Figure 3.

Interestingly, most of the Rydberg states retain their identity (as follows from the wave function analysis and calculated quantum defects) despite the increased size of the core. Moreover, the interactions between the Rydberg states from the two manifolds are negligible, despite their close energetic proximity. We attribute this weak mixing between the two Rydberg manifolds to the open-shell character of the core in the $Ry \leftarrow \pi$ states, whose electronic configuration can be described as:

$$2 \cdot |\pi\beta n\alpha Ry\alpha\rangle - |\pi\alpha n\alpha Ry\beta\rangle - |\pi\alpha n\beta Ry\alpha\rangle \qquad (7)$$

One of these three configurations, $|\pi\alpha n\alpha Ry\beta\rangle$, cannot interact with $|\pi\alpha\pi\beta Ry\alpha\rangle$ because it includes spin-flip and is formally doubly excited with respect to $|\pi\alpha\pi\beta Ry\alpha\rangle$. Thus, the coupling between the Rydberg states from these two manifolds is relatively small, even when the character of the Rydberg orbital is the same. The quartet Rydberg states from the $nl_m \leftarrow \pi$ manifold do not, of course, interact with the doublet $nl_m \leftarrow n$ states. Since this weak interaction is specific to radicals, one may expect stronger mixing between multiple Rydberg manifolds in closed-shell molecules.

4.3. CH$_2$Cl: oscillator strengths of electronic transitions to mixed excited states

A nice illustration of the dependence of the electronic transition dipole moment on Rydberg–valence interactions of excited states is provided by the excited states of the CH_2Cl radical. When the photodissociation of CH_2Cl from its lowest excited state (1^2A_1) was studied in a molecular beam [26], it was noticed that [112] in spite of efficient vibrational and rotational cooling by carrier gases, a large fraction of dissociation products appeared with c.m. kinetic energies exceeding the energy allowed for vibrationally *unexcited* ground state radicals. We determined that the CH_2 and Cl products did not come from two-photon processes, and their relative yields were higher than
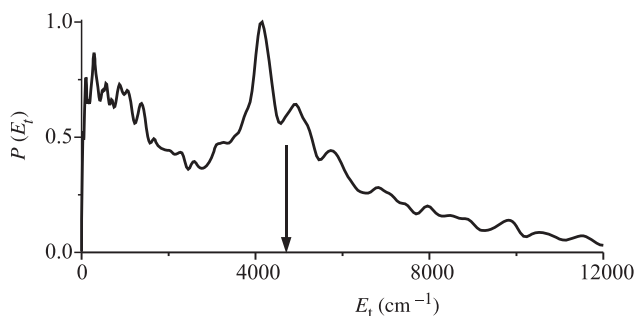
Figure 4. Photofragments c.m. kinetic energy distribution $P(E_t)$ obtained in the photodissociation of the CH_2Cl radical at 266 nm. The distribution was derived from an image recorded by monitoring the $Cl(^2P_{3/2})$ fragment by $2+1$ REMPI. The arrow indicates the maximum allowed kinetic energy release according to the thermochemistry for radicals in their ground vibrational state. The bands at higher kinetic energies, separated by $\sim 800\,cm^{-1}$, correspond to excited vibrational levels of the parent CH_2Cl radical.

predicted based solely on the thermal 'hot band' population of vibrationally excited radicals. The signal intensities indicated that there was a significant enhancement in absorption probabilities for vibrationally excited radicals.

In order to ascertain that products with kinetic energy in excess of the maximum allowed by the thermochemistry were correlated with vibrationally excited radicals, experiments with Ar as a carrier gas, which is known to relax rotational states efficiently, were carried out [26]. Figure 4 shows the c.m. kinetic energy distribution (KED) obtained by monitoring $Cl\ (^2P_{3/2})$ fragments from the dissociation of CH_2Cl at 266 nm in Ar carrier gas. A structure is discernible with $\sim 800\,cm^{-1}$ separation between bands, close to the frequency of the C–Cl stretch in the ground electronic state of CH_2Cl. This 'hot band' component in the translational energy distributions was observed in dissociation at 247–312 nm, i.e. at the red wing of the $1^1A_1 \leftarrow 1^1B_1$ absorption band.

However, high vibrational temperature in the ground electronic state of the radical alone could not explain the observed enhancement. The C–Cl vibrational structure in the translational energy distribution indicated a large geometrical change in the C–Cl coordinate between the ground and 1^2A_1 state. Therefore, *ab initio* calculations of the PES along the C–Cl bond-breaking coordinate and transition dipole moments were carried out for the ground and the two lowest excited states, 1^2A_1 and 2^2A_1. Total energies, equilibrium properties, transition dipole moments and average sizes of the electron density were calculated for the 1^2B_1 ground state and the two lowest $^2A_1$ excited states: the valence state 1^2A_1 ($\sigma^*_{CCl} \leftarrow \pi^*_{CCl}$) and the 2^2A_1 ($3s \leftarrow \pi^*_{CCl}$) Rydberg state [26]. The calculated PESs and dipole strengths of the transitions were used to estimate vibrational overlaps and to calculate Franck–Condon factors.

For ground-state CH_2Cl, we found that the unpaired p electron on carbon interacts with the chlorine lone pair, which is close in energy, resulting in an additional half π bond between C and Cl (Figure 5). This yields a stronger C–Cl bond in the radical relative to the closed-shell compound [21,113]. In the Franck–Condon region, the valence 1^2A_1 state arises from promotion of the unpaired electron in the π^*_{CCl} antibonding orbital to the σ^*_{CCl} antibonding orbital. Therefore, in this excited state a full π bond exists but the σ-bond
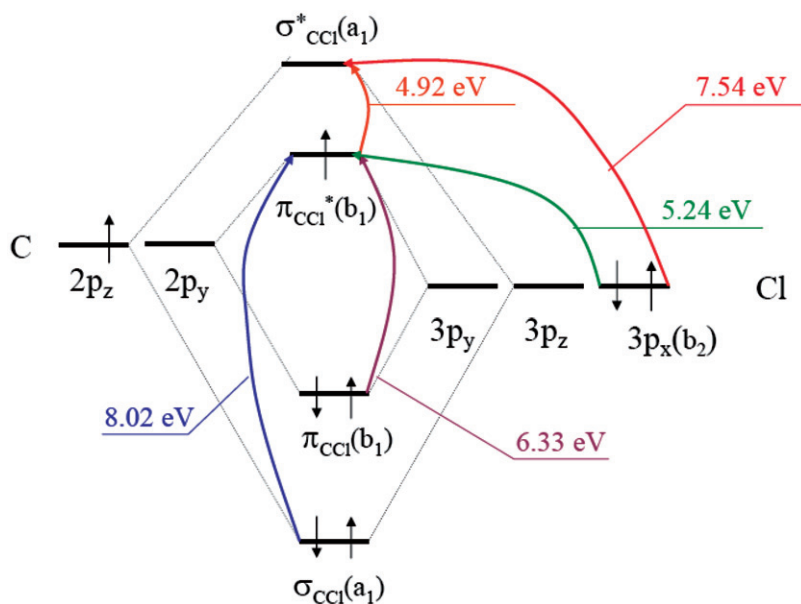
Figure 5. [Colour online] Molecular orbital picture of the bonding and character of valence states in CH_2Cl. The 3s orbital is located higher in energy than σ_{CCl}^* and is not shown. The main electronic transitions and their energies are indicated.

order decreases, and a planar structure with an elongated C–Cl bond relative to the ground state is preferred. Also, the C–Cl stretch vibrational frequency in 1^2A_1 is lower, while the out-of-plane vibrational frequency is considerably higher than in the ground state (due to the decrease in σ-bond order and the increase in π-bond order, respectively). Similar types of changes take place in the Rydberg 2^2A_1 (3s) state, which also involves promotion of an electron from the π_{CCl}^* orbital, but this time to a Rydberg 3s orbital [21].

The results suggest that the minimum energy path for C–Cl bond-breaking on the lowest excited PES is close to a pure C–Cl stretch motion, and other degrees of freedom can be considered frozen. Therefore, in the calculations of the PES along the C–Cl coordinate, the distances of the other two internal coordinates were fixed at the ground state equilibrium values. The resulting adiabatic potential energy curves are shown in Figure 6.

The intriguing feature of the adiabatic 1^2A_1 curve shown in Figure 6 is its shelf-like shape in the vicinity of the ground state equilibrium geometry (i.e. in the Franck–Condon region), which results from Rydberg–valence interactions. Note that similar shapes of excited state potentials have been observed in alkali atom dimers [114–117]. Also, the dipole strength of the transition to this state increases in going from $\sim 1.8\,\text{Å}$ to $\sim 1.6\,\text{Å}$ C–Cl distance (Figure 7). These sharp changes in transition dipole moment contribute to the observed enhancement in the absorption probability for vibrationally excited CH_2Cl, as described further.

In the calculations, we used the size and spatial asymmetry of electron density along the C–Cl stretch to identify changes in electronic state character. We found that at large C–Cl separations ($\sim 1.8\,\text{Å}$) the lowest excited state has a valence character, whereas the
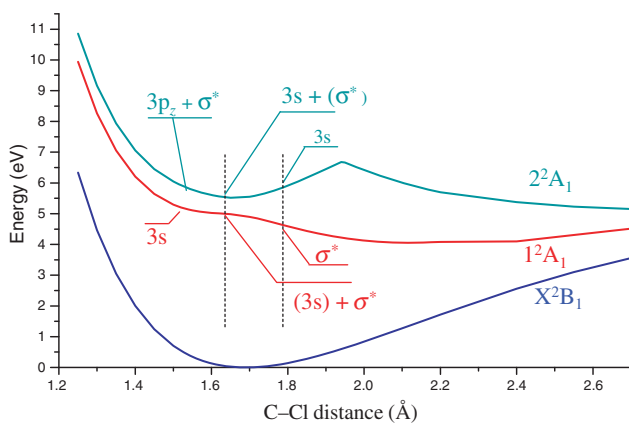
Figure 6. [Colour online] Changes in character and mixing in the 1^2A_1 and 2^2A_1 electronic states of CH_2Cl along the C–Cl stretch coordinate. The two vertical lines indicate the Franck–Condon region.
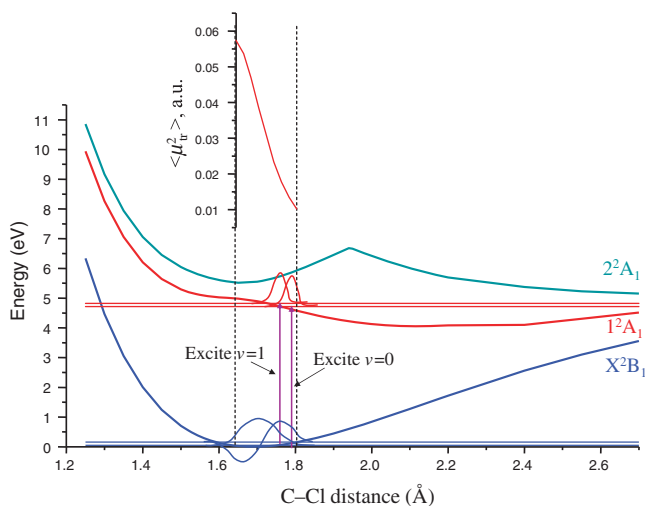
Figure 7. [Colour online] Efficient 'hot band' excitation in CH_2Cl results from a combination of nuclear Franck–Condon factors and changes in transition dipole moment with C–Cl bond distance. When excitation takes place from the ground vibrational state of CH_2Cl, both the Franck–Condon factor and the electronic transition moment, which is depicted at the top of the figure, are small. When a higher vibrational level is excited at the same energy, the Franck-Condon factor is larger and excitation takes place at shorter C–Cl distances, where the transition moment is larger as well. See the text for details.

second excited state has a predominant 3s character. At the ground state geometry (Franck–Condon region; $\sim$1.69 Å) the two states are already mixed, but still retain their identities. At yet shorter C–Cl bond lengths ($<$1.6 Å), the lower state acquires increasingly larger 3s Rydberg character, while the upper state becomes a mixed valence–Rydberg $3p_z$ state. Thus, in effect three-states interactions (valence, 3s, $3p_z$) are manifest in the adiabatic

potential curves of the 1^2A_1 and 2^2A_1 states along the C–Cl coordinate. The transition dipole moment to 1^2A_1 starts decreasing at $\sim 1.6\,\text{Å}$ because of its increasing 3s character.

The electronic transition probability is proportional to the square of the transition dipole moment. However, two factors contribute to the overall transition probability: the spatial overlap of the initial and final vibrational functions (Franck–Condon factor) and the value of the electronic transition dipole moment in the region of maximum spatial overlap. Because the transition dipole to the 1^2A_1 state is strongly influenced by the C–Cl bond length, we limit our qualitative discussion to the 1D potential energy curve along this coordinate.

The enhanced probability for 'hot band' excitation was simulated by calculating the Franck–Condon integrals for the ground and 1^2A_1 states for Morse and Airy wave functions, respectively. This was done for the same range of photon energies used in the experiments. By shifting slightly the excited-state curve within the error bars of the calculations ($\pm 0.1\,\text{eV}$; $\pm 0.1\,\text{Å}$) and using the calculated dependence of the transition dipole moment on C–Cl distance, we could get similar enhancements to the observed ones.

We have found that in the low-energy ('red') edge of the absorption band, the turning points on the 1^2A_1 state are reached only at C–Cl distances in the ground electronic state for which the probability density of the ground vibrational level is very small. Moreover, at these long C–Cl distances, the electronic transition strength is also small and therefore the total absorption probability is small. Thus, ground state absorption contributes little to the observed absorption.

At the same excitation wavelengths, two effects conspire to enhance the absorption probability of 'hot' vibrational bands of the ground electronic state. First, the probability densities of the higher vibrational levels at long C–Cl distances are larger than for the ground vibrational state. This increases the vibrational Franck–Condon factor. Second, photons of the same energy absorbed by an *excited* vibrational level reach the turning point on the upper electronic curve at *shorter* C–Cl distances. This increases not only the vibrational Franck–Condon overlap, but also the electronic dipole strength (Figure 7). The result is a strong increase in absorption probability for 'hot bands'. The enhancement is expected to be largest at the longest wavelengths, as indeed observed experimentally. At shorter wavelengths the 1^2A_1 curve can be reached efficiently from the ground vibrational state at the equilibrium C–Cl distance, and therefore the contribution of the ground vibrational level will start to dominate.

We conclude that Rydberg–valence interactions in the two excited states of CH_2Cl cause changes in the shape of PESs and alter transition dipoles as a function of C–Cl distance. Such Rydberg–valence interactions are common in bond breaking, especially in radicals with low-lying valence and Rydberg states [7,21,118].

4.4. *Trends in electronic absorption in the $CH_3 \rightarrow CH_2F \rightarrow CH_2Cl$ series*

In this section we show how specific molecular orbital interactions can affect the order of valence and Rydberg states in the electronic spectra of halogen-substituted methyl radicals. Figure 8 shows vertical electronic state orderings and oscillator strengths for the three radicals. The spectra are strikingly different; note the increased density of states in the $CH_3 \rightarrow CH_2F \rightarrow CH_2Cl$ series, and changes in state ordering and transition intensities.
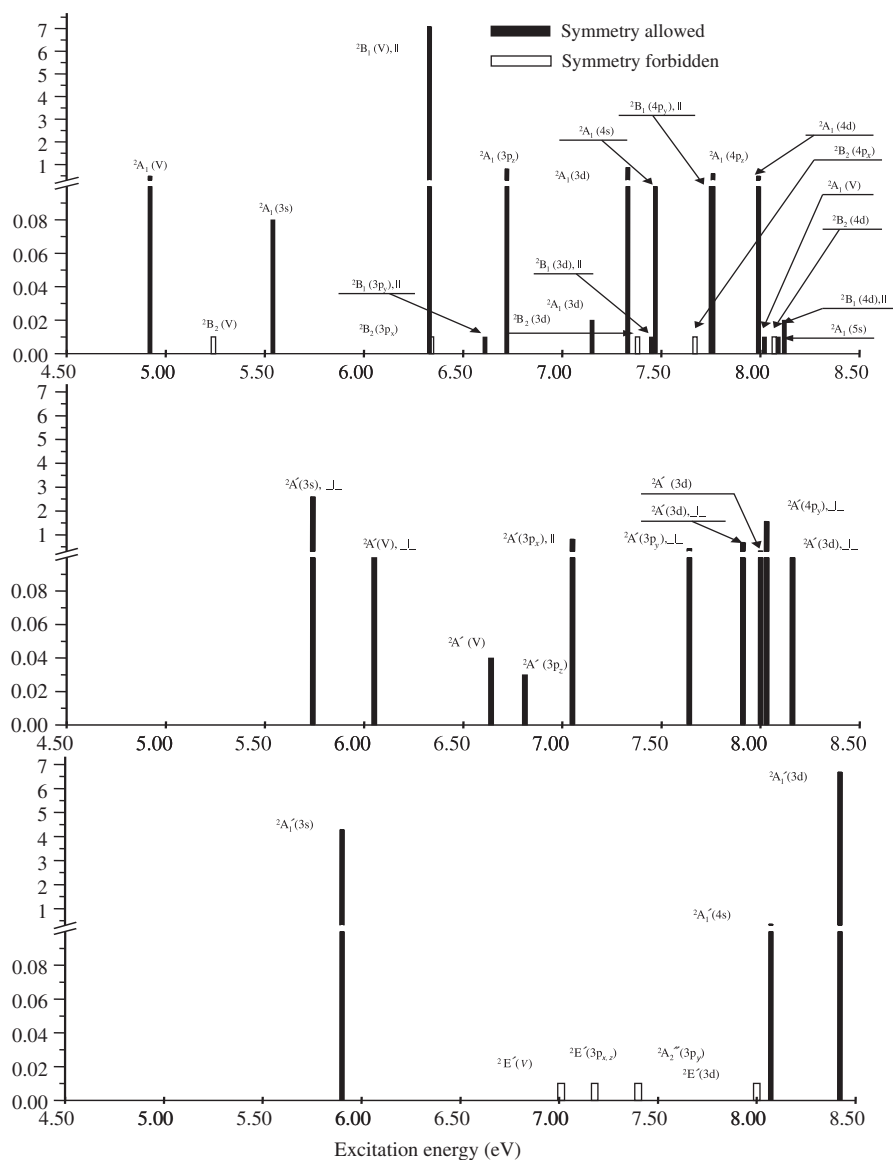
Figure 8. Vertical excitation energies for CH_2Cl (top panel), CH_2F (middle panel), and CH_3 (bottom panel). Intensities of the transitions are proportional to the oscillator strengths (no Franck–Condon factors are taken into account). Empty bars show positions of forbidden transitions, i.e. those for which the oscillator strength is zero due to symmetry. Transitions are defined as parallel when the transition dipole moment is parallel to the CX bond, and perpendicular otherwise. Reprinted with permission from [21]. Copyright (2001), American Institute of Physics.

We show below that these differences are due to changes in the character of the low-lying valence states, whereas the Rydberg states of all three radicals are quite similar. The electronic configuration of the ground ($1^2A''$) state of the CH_3 radical is:

$$(1a_1')^2(2a_1')^2(1e')^4(1a_2'')^1, \tag{8}$$

where $1a_1'$ is the carbon core orbital, $2a_1'$ and $1e'$ are totally symmetric and doubly degenerate combinations of the localised σ_{CH} bonds, respectively, and $1a_2''$ is the singly occupied $2p_y$ orbital.

Figure 8 (bottom panel) shows vertical excitation energies for CH_3. The lowest excited valence state involves excitation from a bonding σ_{CH} orbital to a half-occupied p_y orbital on carbon, located at 7.01 eV. The rest of the states in this energy interval are Rydberg states involving promotion of the unpaired electron.

The character of the lowest Rydberg state is very similar in all three radicals. It derives from a promotion of the unpaired electron to the 3s Rydberg orbital. The excitation energies for this Rydberg state appear to be surprisingly insensitive to the core cation (5.90 eV in CH_3, 5.74 eV in CH_2F and 5.54 eV in CH_2Cl). A similar result holds for the 3p Rydberg states as well: the excitation energies for all three radicals lie within 1 eV, the differences being smaller between CH_3 and CH_2F (about 0.4 eV). Thus, not only the nature but also the excitation energies for the low-lying Rydberg states are similar in all three radicals. The transition strengths are very different due to symmetry imposed selection rules, i.e. the $B_2 \leftarrow B_1$ transition is forbidden in C_{2v}, and the $A_2' \leftarrow A_2''$, $A'' \leftarrow A_2''$, $E' \leftarrow A_2''$ and $A_1'' \leftarrow A_2''$ ones are forbidden in D_{3h} symmetry.

The valence states, however, are very different. Figure 5 shows the relevant MOs and the character of the valence excited states in CH_2Cl. Because the chlorine lone pair is energetically close to the carbon $2p_z$ electron, a partial double C–Cl bond is formed. This gives rise to several low-lying valence excited states that are not present in CH_3. In CH_2F, the lone pair on fluorine is too low in energy to form a partial bond with carbon, and consequently the number of low-lying valence excited states is much smaller. Thus, the number of low-lying valence states increases in going from CH_3 to CH_2F, and then to CH_2Cl. The key factors determining the character and excitation energies of the valence states are the presence of the lone pairs on halogen and how strongly they are bound to the halogen. Referring to the valence states in CH_2F and CH_2Cl, although the nature of the two lowest valence states is similar, the lowest valence state in CH_2F lies more than 1 eV above the lowest valence state in CH_2Cl.

In summary, trends in Rydberg–valence interactions in CH_2X are different from the ones observed in substituted vinyl radicals. In the former case, the Rydberg states are rather similar in all radicals and the valence states are vastly different, whereas in the latter series the valence states retain their vinyl-like character and the Rydberg states exhibit systematic changes.

5. Rydberg–ion core interactions

5.1. *Quantum defects of Rydberg states of vinyl radicals: a closer look*

In this section, we examine how the interactions of the Rydberg electron with the cation core of the vinyl and the substituted vinyl radicals discussed in Section 4.2 infuence

the value of the quantum defect δ. Despite the repulsion of the valence electrons, there is a non-vanishing probability to find the Rydberg electron in such proximity to a heavy nucleus that it 'feels' its higher positive charge, resulting in a positive δ in Equation (1). We distinguish below between the separate series of Rydberg states arising from promotion of an unpaired nonbonding electron n and a π electron in the double bond to nl_m Rydberg orbitals (note the different meanings of n in this notation).

5.1.1. *Changes in quantum defects for the $nl_m \leftarrow n$ states*

Figure 9 presents a summary of quantum defects for the 3s and the three components of the 3p Rydberg states of vinyl, propenyl and butenyl radicals, along with the corresponding changes in IEs and excitation energies upon substitution of hydrogen with methyl (ethyl in case of 1-buten-2-yl) groups [12]. The general trend is that δ decreases as the system size increases, which leads to a slower decrease in excitation energy relative to the drop in IE for larger substituents. Though counterintuitive, it appears that Rydberg states of larger radicals become more hydrogen-like. We attribute this behaviour to a more efficient shielding of the nuclei in larger systems due to the increased number of the core electrons.

The most intriguing result is the large quantum defect for the $3p_x$ (directed along the C–C bond) Rydberg state of vinyl, $\delta = 0.76$ compared to $\delta = 0.69$ in CH_3, and the sharp drop in δ for propen-1-yl and propen-2-yl (by about 0.16), which leads to increased excitation energy for propen-1-yl despite the decrease in IE (Figure 3). The NBO analysis [119] of the electron density for the $3p_x$ state reveals a large weight of carbon 2s orbitals in the Rydberg orbital (occupied by the excited electron) in vinyl, but not in propen-1-yl and propen-2-yl, and this reflects ion core interactions as explained further.

Analysis of the EOM-CC wave functions does not reveal substantial mixing of the valence and the 3s or 3p Rydberg states, which would manifest itself in excitations shared by two or more EOM-CCSD target states. This does not exclude, of course, Rydberg–valence interactions due to the mixed Rydberg–valence character of the Hartree–Fock MOs that reflect the diffuseness of the valence orbitals due to electron repulsion. Thus, we distinguish between the mixing of many-electron states and mixing of one-electron states. The large quantum defect for the $3p_x$ state of vinyl cannot be explained by mixing of Rydberg and valence electronic states.

To understand this quantum defect, we performed NBO [119] analysis of the 3p Rydberg state electron density and visual analysis of the relevant MOs. The analysis demonstrates that about half of the positive charge in the cation core is distributed among the hydrogens. Due to the high polarisability of the C–H bonds, the carbons effectively strip the hydrogens off of their electrons, thus acquiring a negative charge. The MO analysis shows that the orientation of the in-plane $3p_{x,y}$ components in the radicals is determined by the anisotropy of the potential created by the positively charged hydrogens. This is why one of the 3p components ($3p_x$ in our notation) is directed along the line connecting the two far-most carbons in the radicals of C_s symmetry (vinyl, propenyl and *trans*-2-buten-2-yl).

Contrary to atoms, the quantum defect in molecules depends on the charge distribution in the cation core. To explain the role of this charge distribution, we consider two model systems: the methyl and methylene radicals. It is known that δ for the in-plane components of the 3p Rydberg states in methyl (~ 0.7) is larger than for the

δ
0.98
0.76
0.69
0.54

IP 0.35
3s 0.17
$3p_x$ −0.04
$3p_y$ 0.32
$3p_z$ 0.29

IP 0.84
3s 0.61
$3p_x$ 0.43
$3p_y$ 0.70
$3p_z$ 0.72

IP 0.97
3s 0.58
$3p_x$ 0.48
$3p_y$ 0.82
$3p_z$ 0.86

δ
0.92
0.60
0.67
0.51

δ
0.90
0.59
0.62
0.47

IP 0.77
3s 0.50
$3p_x$ 0.66
$3p_y$ 0.63
$3p_z$ 0.71

IP 0.28
3s 0.06
$3p_x$ 0.19
$3p_y$ 0.25
$3p_z$ 0.28

IP 0.13
3s −0.03
$3p_x$ 0.05
$3p_y$ 0.12
$3p_z$ 0.14

δ
0.82
0.54
0.60
0.47

δ
0.84
0.55
0.61
0.48
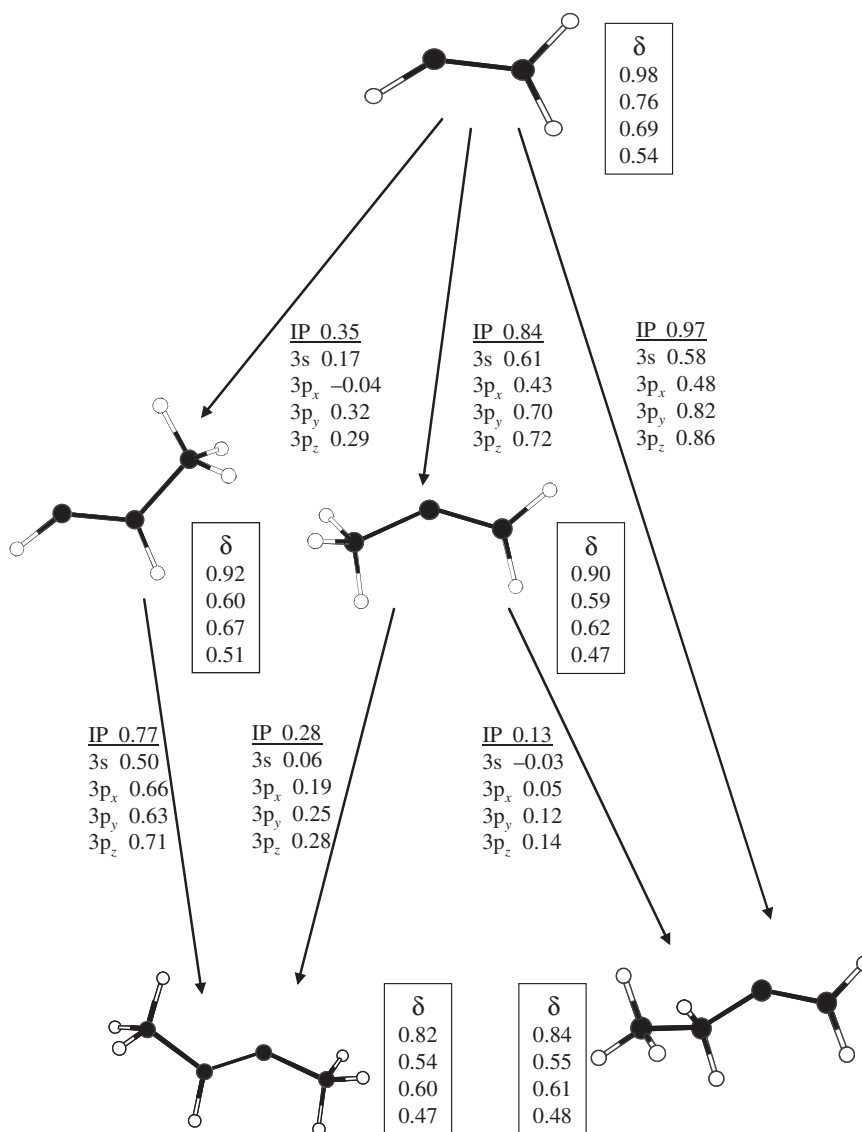
Figure 9. Quantum defects δ for the $nl_m \leftarrow n$ Rydberg states of vinyl and substituted vinyl radicals. Arrows connect species that differ by a single substitution of a hydrogen by a methyl or ethyl group. Next to the arrows, the differences in IEs, and in the excitation energies for the connected species are shown. The boxes show the corresponding changes in δ, written in the order (from top to bottom): 3s, $3p_x$, $3p_y$ and $3p_z$. Reprinted with permission from [12]. Copyright (2006), American Chemical Society.

out-of-plane component ($\sim$0.6) [120], which is close to a free carbon atom. The large δ's for the in-plane components can be explained by the finite dimension of the molecule in the plane. Since the positive charge of the methyl cation is distributed over a finite area, the maxima of the in-plane Rydberg electron wave function tend to approach the centre of the

charge distribution, which is the carbon atom, resulting in a higher probability of finding a Rydberg electron near the carbon nucleus. Note that both the in-plane and out-of-plane Rydberg 3p electrons must have a node on the carbon nucleus in D_{3h} symmetry.

In methylene, the δ's are 0.77 for the $3p_x$ state (in-plane, perpendicular to the symmetry axis), 0.64 for the $3p_y$ state (in-plane, parallel to the symmetry axis) and 0.60 for the $3p_z$ state (perpendicular to the molecular plane) (see footnote 45 in [12]). The larger δ for the $3p_x$ state of methylene relative to methyl is due to the fact that the positive charge of the methylene cation core is distributed mainly in the x direction, whereas in methyl it is spread in the two dimensions of the molecular plane. Note that δ for the $3p_x$ Rydberg state of methylene is almost the same as in vinyl. The important role of the charge distribution in determining δ for the in-plane 3p Rydberg states of methylene and methyl is confirmed by the fact that the sum of these δ's is almost the same in both radicals (2.01 in methylene and 2.00 in methyl). Also, the sum for methylene depends only slightly on the H–C–H angle.

Thus, similar to methylene, we explain the large (0.76) quantum defect for the $3p_x$ Rydberg state of vinyl, which is directed mainly along the C–C bond, by the distribution of the cation core's positive charge along the molecule. In the y direction, the charge distribution in vinyl is similar to that of methyl, and it makes δ for the $3p_y$ Rydberg state of vinyl (0.69) close to δ for the in-plane 3p Rydberg state components of methyl (0.7).

There is another effect that may contribute to the large δ for the $3p_x$ state of vinyl, namely, the centre of the charge distribution (and consequently the nodes of the Rydberg electron wave function) no longer coincides with the carbon nuclei. This further increases the probability of finding the Rydberg electron on the carbon nuclei as confirmed by the increase in δ for larger αCC angles (up to 0.86 for αCC $= 180°$), contrary to methylene, in which it changes only slightly upon increase in the H–C–H angle. This is also confirmed by the increase of the α-C 2s orbital contribution to the Rydberg NBO orbital as the αCC angle increases.

In propen-1-yl or propen-2-yl, as we substitute α- or β-hydrogens with a methyl group, the positive charge distributed along the cation core is more effectively screened by the electrons on the carbon σ bonds. This results in a much smaller penetration of the Rydberg electron into the carbon nuclei, reflected by the large decrease in the quantum defect.

Another interesting observation is the larger decrease in δ relative to vinyl for the $3p_y$ Rydberg state of propen-2-yl compared to propen-1-yl ($\delta = 0.62$ *vs.* 0.67 relative to 0.69 in vinyl). We attribute this difference to the presence of two σ bonds connecting α-C to the other carbons in propen-2-yl *versus* one in propen-1-yl, which results in a more effective screening of α-C with electrons. Moreover, due to the partial positive charge on the hydrogens, the $3p_y$ Rydberg electron in propen-2-yl tends to move around α-C from which it was removed, which is not the case in propen-1-yl (see Figure 1 from [12]).

5.1.2. *Quantum defects in Rydberg $nl_m \leftarrow \pi$ states*

The $nl_m \leftarrow \pi$ manifold is derived from excitations form the doubly occupied π orbital and is similar to the Rydberg manifold in ethylene. It includes both doublet and quartet Rydberg states.[3] Interestingly, δ for the $3p_x \leftarrow \pi$ quartet state of vinyl is large (0.70), and decreases sharply in propen-1-yl ($\delta = 0.55$) and in propen-2-yl ($\delta = 0.54$), very similar to the $3p_x \leftarrow n$ states.

The vertical excitation energies for the triplet $3p_x \leftarrow \pi$, $3p_y \leftarrow \pi$ and $3p_z \leftarrow \pi$ transitions in ethylene are 7.95 eV, 7.94 eV and 8.21 eV, respectively, and the IE is 10.56 eV (see footnote 46 in [12]). This gives $\delta = 0.72$ for the in-plane 3p components, which is almost the same as δ for the in-plane 3p components of the methyl radical, indicating similar cation core positive charge distributions in ethylene and methyl. The calculated quartet $3p_x \leftarrow \pi$ excitation energy for vinyl is the same as the triplet $3p_x \leftarrow \pi$ excitation energy for ethylene (7.95 eV). Also, the IE to reach the lowest triplet cation state of vinyl is 10.53 eV, which is very close to the IE of ethylene, 10.56 eV. However, the corresponding IE to reach the lowest singlet cation state of vinyl is higher, 11.30 eV. The reason why the higher-multiplicity cation and the $3p_x \leftarrow \pi$ excited state energies of vinyl are similar to those of ethylene is also the reduced Coulomb repulsion between an electron in the half-filled orbital and the remaining electron in the π bonding orbital. Note that although this reduction in Coulomb repulsion lowers the quartet $3p_x \leftarrow \pi$ state of vinyl relative to the corresponding doublets, the penetration of the Rydberg electron into the cation core ($\delta = 0.70$) is less than in the case of the $3p_x \leftarrow n$ excitation ($\delta = 0.76$).

In conclusion, the two Rydberg manifolds in substituted vinyl radicals retain their identity and follow a systematic decrease of IEs with the radicals' size, as predicted by Equation (1). Due to the open-shell character of the $nl_m \leftarrow \pi$ manifold, the interactions between the two manifolds are weak, despite their close energetic proximity and similarity of the target Rydberg orbitals. Variations in quantum defects reveal differences in Rydberg–core interactions in these radicals. Analyses of quantum defects for the 3p states from both manifolds suggest that the quantum defects are determined by the geometry-dependent charge distribution within the cation core.

5.2. *Vibrational frequencies and ion–core interactions in 3p Rydberg states of diazomethane*

Ion–core interactions in low-lying Rydberg states can affect not only quantum defects but also geometries and vibrational frequencies. A good example is the 3p Rydberg states of diazomethane, CH_2N_2 [101]. In diazomethane, changes in structure and trends in normal mode frequencies in the ground states of the neutral and ion, and the 2^1A_2 ($3p_y$) and 2^1B_1 ($3p_z$) Rydberg states are consistent with removing an electron from a bonding π_{CN}-orbital that also has an antibonding character with respect to NN. Ionisation or electronic excitation to Rydberg states results in elongation of the CN bond and a slight contraction of the NN bond. The resultant changes in structure and vibrational frequencies can be explained by simple molecular orbital considerations in combination with NBO analysis. In addition, the interactions of the Rydberg electron with the ion core can explain differences in structure and vibrational frequencies between the 2^1A_2 ($3p_y$) and 2^1B_1 ($3p_z$) Rydberg states and the cation.

We first discuss the changes in geometry as seen in electronic structure calculations. The $3p_y$ Rydberg orbital is localised in the plane of the molecule perpendicular to the principal rotation axis (Figure 2). Its electron density is greatest on top of the hydrogen atoms and the C and middle N (directly bonded to C) atoms. The A_2 symmetry imposes a nodal plane along this axis. The 2^1A_2 ($3p_y$) state differs from the cation mostly in the opening of the HCH angle ($129.91°$ relative to $127.80°$ in the cation). The NBO analysis of the electron density of both states reveals that about half of the $+1$ charge of the nuclear
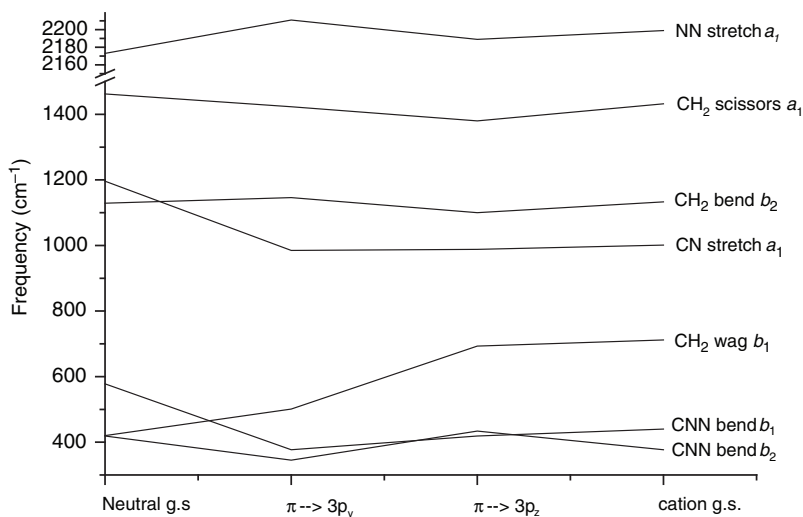
Figure 10. Harmonic vibrational frequencies of the neutral and cation ground states of diazomethane, and of the $^2A_2$ ($3p_y$) and $^2B_1$ ($3p_z$) excited Rydberg states. Reprinted with permission from [101]. Copyright (2007), American Chemical Society.

core is accommodated by the hydrogens. The lobes of the $3p_y$ orbital, located directly on the hydrogen atoms, can interact with the positively charged hydrogen atoms. The larger HCH angle in the 2^1A_2 ($3p_y$) state is thus attributed to the increased electron density along the CH bonds. The $3p_y$ orbital does not affect the CN bond in a similar way due to symmetry restrictions, so the net effect is to increase repulsion between the hydrogens.

A similar argument explains the decrease in the HCH angle in the 2^1B_1 ($3p_z$) state relative to the cation (124.74° compared to 127.80°). The occupied $3p_z$ orbital has electron density centred along the CNN axis, with one lobe centred directly in the space between the two hydrogens, while the other located on the terminal nitrogen, which appropriates almost all of the remaining total nuclear positive charge (Figure 2). Thus, the orientation of the $3p_z$ Rydberg orbital allows its electron density to overlap with the centres of positive charge in the nuclear core, and the HCH angle decreases to maximise this interaction. The $3p_z$ orbital, which has a node on the central nitrogen, can donate density along both the CN and NN bonds; hence, these bonds are contracted relative to the cation.

We now turn our attention to the associated trends in vibrational frequencies. Because of the good agreement between theory and experiment for CH_2N_2, $CHDN_2$ and CD_2N_2 for all the neutral and ionic levels studied experimentally [101], we rely on trends seen in the calculations for the ground state neutral and cation, and $3p_y$ and $3p_z$ Rydberg states of CH_2N_2. The vibrational frequencies are depicted in Figure 10. Only modes below $3000 \, \text{cm}^{-1}$ are shown, because the frequencies of the symmetric and asymmetric CH stretches do not vary significantly with electronic excitation/ionisation.

To explain the observed trends in vibrational frequencies in ionisation and Rydberg excitation, the affected vibrational modes are divided into two groups: (i) those that involve displacements mainly along the CNN framework (CN and NN stretches, and CNN bends) and (ii) those with displacements primarily in the CH_2 moiety (CH_2 wag, rock and bend). For the different electronic states, trends in the first group are mostly due
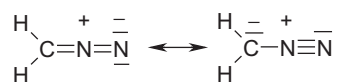
Figure 11. The two resonance structures of diazomethane.

to the effect of lower CN and NN bond orders upon excitation/ionisation, while those in the second are due to the interaction between the positively charged hydrogens and the Rydberg electron density, and the hybridisation of the carbon. Within each group, marked differences are observed between the in-plane and out-of-plane modes.

The four modes that comprise the first group are the CN and NN stretches (both a_1), and the b_1 and b_2 CNN bends. The CN stretch frequency decreases by the removal of an electron from the HOMO π orbital; whether this electron is ionised or placed in a Rydberg orbital has almost no effect on the frequency. The changes in vibrational frequencies involving CNN motions are consistent with these changes in bond order. Reducing the order of the π bond leads to a strong decrease in frequency of the out-of-plane b_1 CNN bend (ν_5) mode in the Rydberg states as well as the cation; i.e. the in-plane Rydberg orbitals provide no additional contribution relative to the cation.

In contrast, the in-plane b_2 CNN bend (ν_6) shows a strong frequency change between the two Rydberg states, which is complementary to that in the analogous mode in the second group, i.e. the b_2 CH_2 bend (rock). For the $3p_y$ state the CNN bending frequency drops significantly with respect to the neutral, whereas the CH_2 bend mode increases slightly. For the $3p_z$ state the CNN bend frequency increases relative to its value in the 2^1A_2 ($3p_y$) state to above the frequency of the neutral, whereas the CH_2 bend decreases to below the value in the neutral. For the cation the CNN mode frequency is lower than in the 2^1B_1 ($3p_z$) state, falling again below the neutral value, while the CH_2 bend increases and is the same as in the neutral.

The largest difference within both modes occurs between the 2^1A_2 ($3p_y$) and 2^1B_1 ($3p_z$) states (Figure 10). For the in-plane CNN bend, the displacement moves the CNN framework off the nodal plane and into the electron density of the $3p_y$ orbital in the yz-plane. However, this displacement moves the atoms out of the density of the $3p_z$ orbital, which is hindered by the donation of electron density into the CN and NN bonds. Consequently, the frequency of this vibration is significantly higher in the 2^1B_1 ($3p_z$) state than in the 2^1A_2 ($3p_y$) state.

Finally and quite surprisingly, the frequency of the CH_2 out-of-plane wag (ν_6) *increases* significantly upon excitation/ionisation. The reason for this is the competition between the two resonance forms in the ground-state wave function of diazomethane and the change in hybridisation of the carbon induced by ionisation/electronic excitation. The two resonance structures are ionic and have positively charged central nitrogen, with the negative charge localised on either the terminal nitrogen or the carbon atom (Figure 11). They differ by the hybridisation of the carbon: sp^2 *versus* sp^3.

The NBO analysis confirms the competition between the two resonance structures in the ground-state wave function. Removing an electron from *either* of these structures results in sp^2 hybridised carbon, and therefore a reduction in the sp^3 contribution, as confirmed also by the NBO analysis. The increased sp^2 character leads to a stiffer out-of-plane vibration, which is exactly what is obtained in the calculations and experiments.

6. Dynamics on Rydberg states of free radicals

As stated above, Rydberg states are often predissociative and products in their ground electronic states must be generated via non-adiabatic interactions with the valence states. The dynamics is usually complicated, often resulting in multiple dissociation pathways. Moreover, more than one mechanism can lead to the same product channel, and more than one intersection seam may be involved. Therefore, interpreting experimental results requires close collaboration with theory. This situation is common in free radicals whose valence and Rydberg states lie in close proximity, and we choose here two examples for which both experimental and theoretical studies are available, the hydroxyalkyl and ethyl radicals. The dissociation of these radicals involves Rydberg–Rydberg and Rydberg–valence conical intersections. We end by briefly discussing the intriguing case of triple conical intersections that involve simultaneous crossing of three excited PESs.

6.1. *Hydroxyalkyl radicals: dissociation via conical intersections*

In photodissociation of the hydroxyalkyl radicals, conical intersections with the ground state control the branching ratios and fragment internal energy distributions [22–25,121,122]. Electronic structure calculations on the prototype radical CH_2OH show that the lowest four electronic states have a Rydberg 3s, $3p_x$, $3p_y$ and $3p_z$ character. The Rydberg formula is a good starting point for estimating energies of Rydberg states, and deviations often indicate interactions with valence states. In Rydberg states of CH_2X radicals (X = H, halogen), δ for the 3s state is $\sim$1.0 and those for 3p states are in the range 0.6–0.9 [123,124]. The CH_2OH and CH_3CHOH radicals can be generated cleanly in molecular beams by reactions of Cl atoms (produced by 355 nm photolysis of Cl_2) with the corresponding alcohols in a quartz tube attached to the pulsed nozzle [121,122], thereby enabling studies of their photodissociation dynamics.

Although Rydberg states of CH_2OH are bound, they can be strongly predissociative. For example, no minimum could be found for the 3s PES even in high-level electronic structure calculations [24,25]. This is a general feature of low-lying Rydberg states of 2nd-row molecules: their 3s states penetrate into the ion core to such an extent that they are often purely dissociative (e.g. CH_3, C_2H_5)[3,6]. C_2H_5, in particular, provides a good analogue to CH_2OH. Its UV absorption spectrum in the region of excitation to the 3s Rydberg state (230–265 nm) is broad and structureless, while absorptions to the 3p states exhibit characteristic vibronic structure [125] (see also Section 6.2).

6.1.1. *Photodissociation of CH_2OH on the 3s, $3p_x$ and $3p_z$ Rydberg states*

The ground state of the hydroxymethyl radical is described by the configuration ....$(\sigma_{CO})^2$ $(\pi_{CO})^2 (n_O)^2 (\pi_{CO}^*)^1$. The Rydberg states are obtained by promoting the electron in the half-occupied π_{CO}^* antibonding molecular orbital to a Rydberg orbital localised on the carbon atom [126]. This results in a stronger double bond character in CO in the Rydberg states and the cation and a large change in CO bond length and stretch frequency [121,126]. The ground state is nonplanar, conforming to the C_1 symmetry point group [126]. However, because of the shallowness of the CH_2 wag potential, the electronic wave function complies with C_s A'' symmetry, as do the Rydberg states and the cation, and therefore, the electronic transitions are labelled by C_s symmetry [126].
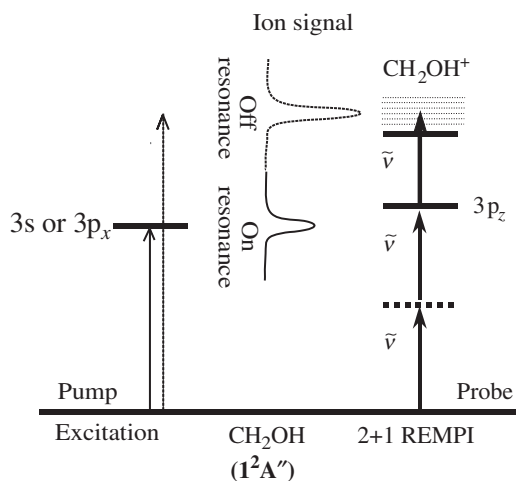
Ion signal

Figure 12. Schematic representation of the depletion method used to identify electronic transitions to dissociative states of jet cooled CH_2OH radicals. When the pump frequency matches an absorption band in the transition to the 3s or $3p_x$ states, the population of the ground state of the radical is reduced. The ground state population is monitored via a $2+1$ REMPI probe signal centered on the origin band of the $2^2A''(3p_z) \leftarrow 1^2A''$ transition. The signal decreases whenever absorption to the 3s or $3p_x$ state precedes $3p_z$ excitation.

The 3s, $3p_s$ and $3p_z$ Rydberg states were accessed by one-photon excitation, but their assignment was difficult because of their short lifetimes and overlap among absorption bands. In the molecular beam, three types of spectra were used for assignment: (a) depletion spectra; (b) H and D photofragment-yield spectra from CH_2OD, with H and D detected by $(1+1')$ REMPI via the L-α transition at 121.6 nm; and (c) $2+1$ and $2+2$ REMPI spectra.

The $2+1$ REMPI spectrum of CH_2OH in the region 41,000–45,000 cm^{-1} shows vibronic bands belonging to the $2^2A''(3p_z) \leftarrow 1^2A''$ transition with an origin band at 41,062 cm^{-1} [121]. A prominent 1600 cm^{-1} vibrational progression in the C–O stretch is identified [126,127], and the lifetime of this state is ~ 0.5 ps [126–128].

The $3p_x$ state origin was located by the depletion method, as shown schematically in Figure 12. The probe laser frequency was fixed at the known $2^2A''(3p_z) \leftarrow 1^2A''$ origin band [127], and the pump laser was scanned in the range 26,000–42,000 cm^{-1}, where the $3p_x$ and 3s states were expected [121]. The population of the ground state was depleted whenever photon absorption occurred, thereby causing an attenuation in the CH_2OH^+ REMPI signal. A vibronic peak at 35,063 cm^{-1} (4.34 eV), observed by both depletion and REMPI, was assigned as the origin band of the $2^2A'(3p_x) \leftarrow 1^2A''$ transition [121]. As expected, the vibrational progressions in transitions terminating in the $3p_x$ and $3p_z$ states were found to be quite similar [121]. All the vibronic bands were broader than those of the corresponding transition to $3p_z$, indicating that $3p_x$ is rapidly predissociating.

No REMPI signal could be detected from the 3s state but, using depletion, a broad and structureless absorption starting at 26,000 cm^{-1} (3.21 eV) and extending as an underlying continuum in the regions of the transitions to $3p_x$ and $3p_z$ was detected. The spectrum

was assigned as the $1^2A'(3s) \leftarrow 1^2A''$ transition [121,129,130]. The assignments of all the electronic transitions were in excellent agreement with *ab initio* calculations [24,25,129,130]. The measured quantum defects for the 3s, $3p_x$ and $3p_z$ were 1.23, 0.94 and 0.65, respectively, all within the respective ranges for other CH_2X radicals [123,124,131].

The lowest dissociation channels, $H + CH_2O$ and $H + HCOH$, correlate only with ground-state CH_2OH, and must be reached by internal conversion from higher Rydberg states, which lie $> 2\,eV$ above the $H + CH_2O$ asymptote. Using the deuterated analogue CH_2OD, yield spectra of H and D photofragments were recorded to distinguish between O–H and C–H bond breaking pathways [22,23,121]. With 3s photolysis near the origin of the absorption (365–318 nm), only the O–D bond-breaking channel was observed, but at shorter wavelengths (< 318 nm) H products were detected as well. The signal from the C–H fission channel increased monotonically with decreasing wavelength, and no sharp change in the H/D ratio was detected when the band origins of the transitions to the $3p_x$ and $3p_z$ states were traversed, pointing to the existence of a common final step in the dissociation [121].

By using core-sampling TOF [92,93], fragment kinetic energy distributions (KEDs) and anisotropy parameters were determined. D photofragments were correlated energetically with the $CH_2O + D$ channel, and their recoil anisotropy parameter, $\beta_{eff} = -0.7 \pm 0.1$, was close to the limiting value of -1 for the perpendicular $1^2A'(3s) \leftarrow 1^2A''$ and $1^2A'(3p_x) \leftarrow 1^2A''$ transitions. Most of the available energy was channelled into translation, with cold formaldehyde as a co-product [22,23].

The KEDs of the H photofragments from C–H and O–H bond breaking in CH_2OH (D) are very different. The results show, in accordance with the thermochemistry, that the C–H bond is much stronger than the O–H(D) bond, and the distributions are broad and isotropic. Out-of-plane motions in the non-adiabatic couplings leading to the HCOH(D) channel are probably responsible for the observations [22,23].

The conical intersection calculations of Hoffman and Yarkony [24] and Yarkony [25] pinpoint pathways for radiationless decay that play a pivotal role in the photodissociation. They provide a qualitative interpretation for the observed behaviour by identifying efficient crossing seams between the 3s and the ground states and between $3p_x$ and 3s.

Specifically, a low-energy crossing seam between 3s and the ground state was found at 2.9 eV at an O–H distance $R(OH) \sim 1.48\,Å$, extended by about 0.5 Å from the equilibrium O–H distance in the ground state. The vertical cone for this intersection greatly promotes radiationless transitions from 3s to the ground state. After the 3s/ground state transition, CH_2OH can dissociate directly to $CH_2O + H$, as a result of the low dissociation energy of this channel (1.3 eV) and the large value of R(O–H) accessed on the ground state, which lies in the replusive region of the ground state PES (beyond the barrier to O–H fission). Our observation of abundant D production for CH_2OD excited near the onset of the transition to the 3s state is consistent with this analysis [121]. The calculations predict that absorption to 3s would be structureless, as confirmed in the experiments.

Although there exist no dynamical calculations for CH_2OH dissociation, Yarkony [25] examined in detail the gradients on the ground state following conical intersections with 3s by looking at the so-called *g* and *h* vectors and the associated nuclear motions that promote surface intersections. He concluded that, in addition to the motion described above, gradients on the ground state can lead to reduction in $R(OH)$, propelling some of the radicals toward the equilibrium geometry of the ground state. This pathway should
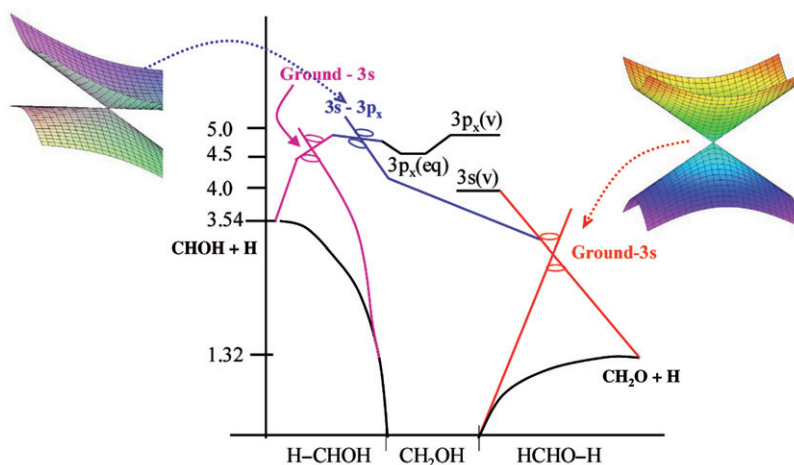
Figure 13. Schematic picture of conical intersections in CH_2OH excited to the 3s state. Intersections between the 3s and the ground state along the O–H and C–H coordinates are shown in red, whereas the intersection between 3s and $3p_x$ is shown in blue. The corresponding vertical and tilted intersection cones are also shown.

lead to unimolecular dissociation on the ground PES, which would be more statistical in nature, providing routes to both C–H and O–H bond fission channels. This analysis underscores the strong effects of gradients near the conical intersections on nuclear motions.

At higher excitation energies, a second conical intersection seam, located along the CH coordinate in the exit channel, is reached on 3s, as shown schematically in Figure 13. This seam, which involves a small barrier relative to HCOH + H, becomes more accessible as the excitation energy increases, thereby explaining the corresponding fast increase in HCOH yield.

According to the calculations [24], when the radical is excited to the $3p_x$ state, it first couples to 3s via a conical intersection (tilted cone), and subsequently to the ground state as described ealier (Figure 13). Because of the proximity of the manifold of 3p and 3s states, Franck–Condon considerations favour sequential couplings between the Rydberg states before coupling to the ground state takes place. In this regard, the cases involving triple conical intersections that have been identified for the allyl and ethyl radicals excited to Rydberg states are noteworthy [132,133] (see also Section 6.2).

Finally, comparison of the TOF distributions obtained in photodissociation of CH_2OD via the 3s and $3p_z$ states shows that the CH_2O internal energy distributions are remarkably different. Whereas O–D bond fission on 3s gives rise to formaldehyde products with little internal energy, this is not the case in dissociation from $3p_z$ [134]. The D fragment KEDs show that the CH_2O fragments are internally 'hot' extending to the full energy range allowed by the thermochemistry [22,23]. The high internal excitations of the products are probably due to out-of-plane motions that couple the $^2A''(3p_z)$ state to the lower Rydberg states of A' symmetry, as well as to nuclear dynamics near the conical intersections regions.
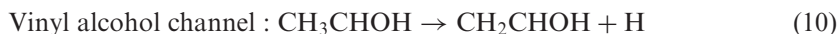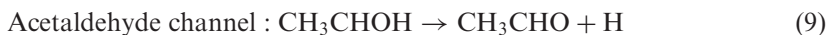
6.1.2. *1-Hydroxyethyl radical: acetaldehyde and vinyl alcohol photodissociation channels*

The next homolog of CH_2OH is the 1-hydroxyethyl radical, CH_3CHOH, which figures prominently in reactions of atoms with ethanol, and the $O + C_2H_5$ and $OH + C_2H_4$ reactions [135–140]. In fact, the three structural isomers, CH_3CHOH, CH_2CH_2OH and CH_3CH_2O are all implicated in the $OH + C_2H_4$ reaction [138], which is important in combusion, and vinyl alcohol formation (C–H fission) has recently been suggested as a significant channel [140]. It was assumed that the three lowest absorption systems would involve excitations to 3s, $3p_x$ and $3p_z$, and that they would have similar quantum defects to those of CH_2OH. However, the existence of additional out-of-plane modes involving the methyl group should increase the efficacy of non-adiabatic couplings in CH_3CHOH, as was indeed found in the measurements [122]. Conical intersection seams might be located along the O–H, C–H and C–CH_3 bond fission coordinates.

The IE of CH_3CHOH is much lower than that of CH_2OH (6.64 *vs*. 7.50 eV) [141–143], but using the Rydberg formula with quantum defects δ similar to those of CH_2OH, the threshold energies for transitions to the 3s and 3p Rydberg states can be predicted.

REMPI and H-photofragment yield spectroscopy were used to assign experimentally the electronic spectrum. Using $2 + 2$ REMPI, a progression of broad bands (width $\sim 100 \, cm^{-1}$) separated by $\sim 1600 \, cm^{-1}$ was identified [122], which in analogy with the narrower bands observed in the hydroxymethyl radical was assigned to a CO-stretch progression (Figure 14). The band origin was placed at 309 nm (4.00 eV, 32,300 cm^{-1}), close to the 296 nm value predicted by the Rydberg formula for the $3p_z$ state. The onset of absorption to the 3s state was found at 510 nm (2.43 eV, 19,600 cm^{-1}), again near its predicted value. The results show that the couplings of the Rydberg states to the ground state are, indeed, much stronger in CH_3CHOH than in CH_2OH.

Following absorption to the 3s, $3p_x$ and $3p_z$ states (520–300 nm), TOF spectra of H and D atoms from CH_3CHOH (D) were obtained and KEDs and recoil anisotropy parameters β were derived [122]. When exciting CH_3CHOH near the onset of the 3s state, one H-photofragment peak, centred close to the maximum of the allowed kinetic energy ($D_0 = 1.1 + 0.1$ eV), was observed. In this region, the recoil anisotropy parameter, $\beta = -0.7 \pm 0.1$, was typical of a perpendicular transition. At excitation energies $> 31,200 \, cm^{-1}$ (3.87 eV), another peak appeared at low translational energies with $\beta \sim 0$ (Figure 15). Its relative intensity increased with excitation energy but its β value did not change. Although the REMPI spectrum from $3p_z$ at > 4.00 eV was structured, the H and D photofragment yield spectra in this energy region were unstructured. On the basis of results obtained with CH_3CHOH (D) it was concluded that (i) throughout the investigated 520–300 nm region, the strongest absorption is to the fast dissociative 3s state and (ii) there were two distinct product channels that yield H atoms:

$$\text{Acetaldehyde channel} : CH_3CHOH \rightarrow CH_3CHO + H \tag{9}$$

$$\text{Vinyl alcohol channel} : CH_3CHOH \rightarrow CH_2CHOH + H \tag{10}$$

The C–CH_3 bond-breaking channel has yet to be observed. H-photofragments from reactions (9) and (10) correspond, respectively, to the observed high and low kinetic energy peaks in the KEDs shown in Figure 15. Even though the thermochemical threshold for reaction (10) was calculated at 1.5 eV [138], products from this reaction were observed only when the excess energy exceeded 2.9 eV. It appears that the pathway leading to
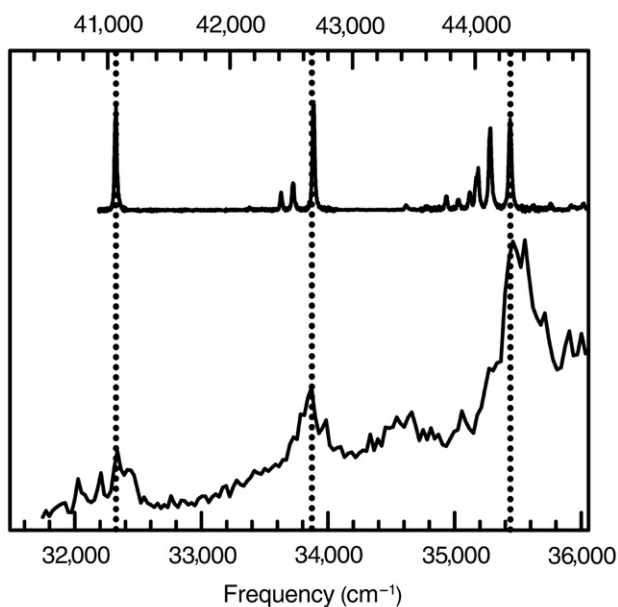
Figure 14. $2+1$ REMPI spectra of CH_2OH (top panel and scale) and CH_3CHOH excited in the region of absorption to their $3p_z$ states. The lowest energy band of each transition is the origin band. Reprinted with permission from [122]. Copyright (2006), American Chemical Society.
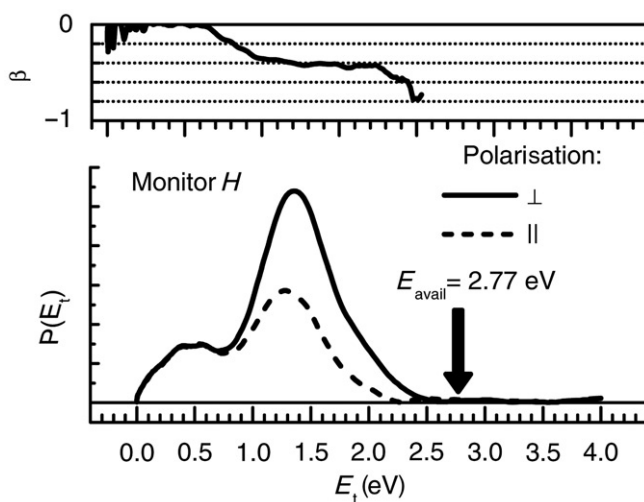
Figure 15. Photofragment c.m. kinetic energy distribution $P(E_t)$ of CH_3CHOH obtained by monitoring H photofragments following excitation to the 3s state at $31,250\,cm^{-1}$ (3.87 eV). The arrow indicates the available energy. The recoil anisotropy parameter β is plotted as a function of E_t in the top panel. Reprinted with permission from [122]. Copyright (2006), American Chemical Society.

reaction (10) has a minimum intersection energy much above the thermochemical threshold for this channel. However, once this energy is exceeded, the dynamics on the upper state PES propel the excited molecules towards both conical intersection seams. The dynamical evolution via the conical intersection for reaction (10) deposits much of the available energy as internal energy of the vinyl alcohol fragments.

From experiment and theory we conclude that the Rydberg formula should hold rather well in the homologous series of CH_2OH, serving as a guide to the absorption spectra of higher hydroxyalkyl radicals whose radical centre is located on C adjacent to OH (1-position).

In addition to the experiments, an electronic structure study of the ionisation of CH_3CHOH and CH_2OH helped explain why the IE of the former is lower by almost 1 eV than the latter. The results show that the decrease in IE results from hyperconjugation effects, with the methyl group destabilising the HOMO of the neutral and stabilising the HOMO of the ion [19].

6.2. *Ethyl radical: non-classical Rydberg states and triple conical intersections*

In the last section we describe briefly work on the photodissociation of the ethyl radical, a prototype for alkyl radicals, in order to highlight two features: (i) the role of non-classical structures of Rydberg states and ions and (ii) the occurrence of triple conical intersections. While the lowest excited states of C_2H_5 are the 3s and 3p Rydberg states, similar to CH_3 and CH_2OH, the situation in C_2H_5 is different because its ground state cation has a non-classical bridged geometry, with a bridging H making a three-membered ring with the two C atoms. The ground state of the neutral radical has C_s symmetry, and in the Franck–Condon region, the open-chain, C_s-symmetry Rydberg states are reached, although the non-classical Rydberg states with C_{2v} bridged geometry are lower in energy (Figure 16) [5].
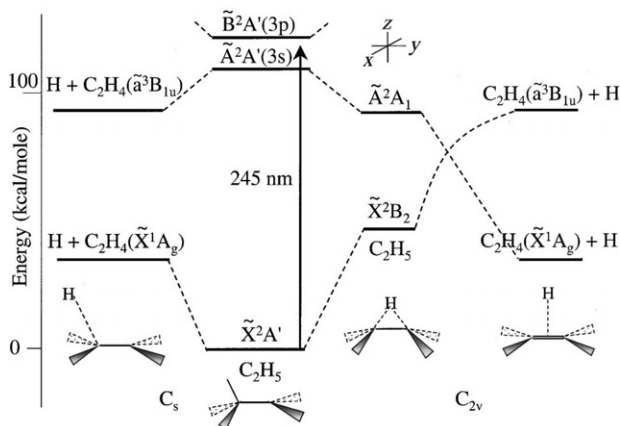

Figure 16. Energy level and correlation diagram of the C_2H_5 photodissociation system in C_s and C_{2v} symmetry. The intersection of the $^2B_2$ and $^2A_1$ states in C_{2v} symmetry becomes an avoided crossing in C_s. Reprinted with permission from [97]. Copyright (2001), American Institute of Physics.

The ethyl radical is fairly weakly bound and thus difficult to produce cleanly and efficiently. Neverthess, it was produced by both pyrolysis and photolysis [97,144–149] and an excellent summary of previous work is given in [5]. Here we focus on the UV photodissociation from the 3s state, which was studied in the 230–265 nm range.

Gilbert *et al.* [144] found that H-atom fragments had predominantly low kinetic energies, implying that the ethylene co-fragments were internally excited, and the angular distributions were isotropic. In addition, they observed that some of the molecules dissociated much more slowly than predicted by statistical theories of unimolecular decomposition (observed rates of the order of $\sim 10^7 \, s^{-1}$). Similar slow rates were observed by Noller *et al.* [15] and Zierhut *et al.*[151] in photodissociation of the 2-propyl and *tert*-butyl radicals. Amaral *et al.* [97] using the HRTOF technique, have identified an additional componenet, namely, fast H-atoms with anisotropic angular distributions ($\beta = 0.5$). From studies of partially deuterated ethyl radicals, it has been deduced that it is the methyl hydrogen that dissociates in all cases [146,147]. Because of its fundamental importance in combusion, several theoretical articles discussed the electronic structure and dissociation mechanism of the radical [152–157].

6.2.1. *Non-classical Rydberg states and non-adiabatic transitions*

Figure 16 displays schematically the energies and geometries of relevant states invoked in the photodissociation of the ethyl radical, as well as several pathways that can lead to H-atom fission [97]. Adding to the complexity in this case is the fact that the bridged, lower-energy C_{2v} structures can be reached from the open-chain C_s states that are excited in the Franck-Condon region. Thus, after excitation to the C_s $1^2A'(3s)$ state the following pathways may lead to H fragments: (1) direct dissociation on the excited 3s C_s state, which correlates with ethylene co-fragment in the triplet state; (2) transformation to the bridged C_{2v} $1^2A_1(3s)$ state, which correlates adiabatically with ground state ethylene; (3) a conical intersection between the 3s and ground state that leads to direct dissociation on the ground state, resulting in fast H atoms and ground state ethylene and (4) conical intersection or any other internal conversion mechanism leading to more statistical dissociation on the ground state PES.

Amaral *et al.* in their interpretation favoured, in agreement with theory [152–154], an initial transformation of the C_s $1^2A'(3s)$ state to the bridged C_{2v} $1^2A_1(3s)$ excited state, followed by direct dissociation on this PES via pathway (2). This is supported by their recoil anisotropy results. They attributed the slow H component to what they refer to as internal conversion to the ground state PES, from which the radical dissociates in a more statistical fashion [97].

Amaral *et al.* point out that the $^2A_1$ and $^2B_2$ surfaces in Figure 16 are connected by a conical intersection, and they suggest that the migration of the H-atom to the bridged position funnels the dissociating flux to the conical intersection region. The authors note that these two states are both A' in C_s symmetry and thus have an avoided crossing. In their description, states of the non-classical bridged structure are active participants in the dissociation via both the direct adiabatic pathway (2) and pathways (3) and (4) that involve conical intersections. This model does not explain why the dissociation is slow.

In a very recent investigation, Hostettler *et al.* [157] exploited direct *ab initio* dynamics calculations on MR-CISD surfaces using the trajectory surface-hopping method with Tully's [158] fewest switches to simulate the photodissociation dynamics. They used an

ensemble of about 5000 trajectories and deduced that the lifetime of the excited state was ∼20 fs. From a detailed examination of the trajectories and the fragments' recoil energies associated with them, they concluded that more than half of the trajectories followed rapid non-adiabatic transitions and prompt dissociation to generate fast H atoms. Another ensemble, resulting from non-adiabatic transitions, led to slow H atoms generated by unimolecular decomposition of hot ethyl radicals on the ground electronic state. This mechanism, which leads to both direct dissociation and an indirect, statistical-like, process, is similar to what Yarkony [25] has inferred for the decomposition of CH_2OH by analysing the g and h vectors. Yarkony, however, did not carry out full dynamical calculations terminating in fragmentation.

In addition, and specific to the ethyl radical, Hostettler *et al.* [157] conclude that the adiabatic pathway (1) participates in the reaction, leading to triplet ethylene and slow H atoms. It is difficult to confirm this pathway experimentally, because the slow H component would overlap with similarly slow H fragments generated by unimolecular decomposition on the ground electronic state (pathway 4). Subtle changes in the recoil anisotropy parameter as a function of kinetic energy release might provide clues.

Hostettler *et al.* [157] point out that the branching ratio between the adiabatic pathway (1) and the non-adiabatic pathways (2)–(4) depends strongly on features of the PES. Therefore, cooperation between theory and experiment will be needed to fine-tune the PESs and interpret the dynamics. The authors do not discuss the role of the non-classical C_{2v} states (Figure 16), though they point out that the transition state for the non-adiabatic transition has a non-classical, bridged structure, and that H-shift in the excited molecule is facile. Thus, how easily the Rydberg states switch between the open-chain and bridged structures is yet to be determined. Likewise, the slow photodissociation rate remains to be elucidated. The trajectory calculations, however, indicate that trapping does not take place on the excited 3s state, which decays rapidly, and must arise in subsequent steps in the evolution of the system to products. Since slow dissociation appears in other alkyl radicals, these observations merit further investigation.

6.2.2. *Triple conical intesections of Rydberg states*

We end this review by touching briefly on the existence and relevance of triple conical intersections [132,133]. For the radicals described in this review, optical excitation often accesses 3s and 3p Rydberg states, which lie in close proximity. In fact, the degeneracy of the three 3p states is removed only by interactions with the nonspherical ion core or with valence states, as described above. Photodissociation in these cases proceeds via conical intersections, and we already discussed the case of hydroxymethyl, in which sequential conical intersections lead to the observed products. In most cases, conical intersections are not required by symmetry and are termed 'accidental' [32]. Can there be cases in which three surfaces intersect simultaneously? In particular, can the degeneracy among the 3p Rydberg states be restored by effecting modest nuclear distortions in the molecule?

Matsika and Yarkony [132,133] have discussed such cases and their importance in free radical dissociation. They point out that when crossings among more than two surfaces are required for dissociation, the intersection between two surfaces may be most efficient at a geometry that is different than the one required for the next sequential intersection, thereby taking the molecule away from the desired geometry. In this regard, triple conical intersections may assist photodissociation. On the other hand, for two-state intersections

the dimension of the intersection surface is $N_{int}-2$, where N_{int} is the number of vibrational degrees of freedom, but this dimension is reduced to $N_{int}-5$ for triple conical intersections, and thus the phase space available for triple intersections is much reduced compared to sequential two-conical intersections. However, when the three surfaces are close in energy and character, the geometrical distortions required to bring them into degeneracy might be modest, and the minimum intersection energy might not be too high. While no experimental evidence exists to confirm triple intersections, knowledge of their location and energy is important when sorting among possible mechanisms.

Matsika and Yarkony have developed efficient search algorithms to identify the energies and geometries of triple conical intersections and the ethyl radical was their first example [132]. The excited electronic states of ethyl were described at the state-averaged MRCI level [53] with no spatial symmetry constrains. The active space was chosen to provide a good description of the five lowest states (ground, 3s, 3p). Using their efficient algorithms, they have identified the geometry and state energies at the triple crossing locations among the 3p states. They find that the key difference between these geometries and the ground state geometry is the contraction of the C–C bond from 1.494 Å to 1.345 Å and extension of one of the methyl hydrogens from 1.096 Å to 1.156 Å. They note that in this geometry, the radical is still clearly molecular, i.e. not close to dissociation. However, at $\sim 52,000\,cm^{-1}$, the energies for the triple intersections are $\sim 5,000\,cm^{-1}$ above the energy of the calculated highest 3p state, and thus, the most likely dissociation mechanism from the 3p states should be sequential conical intersections to finally reach the dissociative state. In general, since many radicals include near-degenerate Rydberg and valence states, the existence of triple conical intersections must be born in mind when analysing results.

7. Conclusions and outlook

In this review we have described several examples that highlight the interactions between Rydberg and valence states and their manifestations, emphasising small organic free radicals. Clearly, much excellent work has not been covered even within this restricted group of radicals, and additional reviews and recent articles describe other radical systems [5,85,159–175]. What we have attempted to convey is the depth and breadth of information that can now be obtained on the evolution of photodissociating radicals and molecules that involve Rydberg states, and the crucial role of collaboration between theory and experiment. A good case in point is the UV photodissociation of the NO dimer, recently summarised in a review article [176], for which interactions between Rydberg and valence states on multiple PESs are crucially important. Experimental studies exploited REMPI, LIF and photoelectron spectroscopies, pair-correlated imaging of state-selected products, time-resolved photoelectron spectroscopy, and femtosecond time-resolved photoelectron–photoion coincidence imaging studies. Likewise, results from several theoretical groups exploiting different methods were required to identify the excited states and their interactions. Only then did it become possible to come up with a comprehensive picture of the photodissociation mechanisms.

Clearly, on the experimental front, many new sophisticated tools can now be brought to bear to elucidate the complex dynamics that transpires in regions of conical intersections of excited molecules. No single group can have all the required wherewithal nor the required experimental expertise. For a comprehensive picture to emerge requires the cooperation

of several groups exploring a broad range of dissociation energies and locations on the PES. This is the reason why comprehensive mechanisms are available only for a few cases. Fortunately, these proof-of-principle experiments (see, e.g. [5,8,68,161,175]) have become a source of optimism that complex molecular processes can be studied at a high level of detail. It has also become clear that Rydberg–valence interactions are important in larger systems, for example, those relevant to biological and environmental processes.

On the theoretical front, parallel progress has been made, but considerable challenges remain. The most difficult problem is how to extend reliable and predictive electronic structure methods such as EOM-CC to tackle much larger systems. Moreover, although electronic structure calculations provide a wealth of important information, the picture is incomplete without dynamics. Ideally, one would like to be able to perform dynamics calculations in full dimensionality using high-level *ab initio* PESs (i.e. generated on-the-fly). This poses additional challenges for electronic structure methodology, as such calculations would involve thousands of *ab initio* calculations. Finally, because electronic transitions often involve interacting states of different character, one needs to depart from classical molecular dynamics and include non-adiabatic transitions, which requires calculation of state couplings and departure from localised trajectories description. While there are impressive examples of methodological developments along these lines, e.g. the multiple spawning method with *ab initio* potentials generated on-the-fly, which has been applied to many excited-state processes in polyatomic molecules (see [177,178] and references therein), significant challenges remain.

As an example of an important problem that highlights electronic structure methodology, consider the recent electron-transfer (or electron capture) dissociation mass spectrometry experiments [7,179]. This technique is used, e.g. to characterise polypeptides. In these experiments, polypeptide fragmentation is initiated by charge exchange between a negatively charged particle and an acidified (i.e. protonated) gas-phase polypeptide. It is believed that the electron attaches initially to a high Rydberg orbital (centred on the positively charged groups) to form an electronically excited hyper-valent radical. Calculation of the cross section for this step requires calculations of couplings between different Rydberg states of the peptide and the negatively charged particle. Although this could be done by using a simple Mulliken–Hush diabatisation scheme from permanent and transition dipole moments (as has been done, e.g. in Ref. [68]), a more detailed description of the process requires calculation of the non-adiabatic couplings between the states of the combined anion-acidified peptide system.

After charge exchange, the attached electron cascades down the Rybderg manifold to the ground-state Rydberg orbital, but a substantial barrier must be overcome before it can transfer to the S–S σ^* orbital to cleave the S–S bond. In contrast, when the cascading electron reaches the lowest excited Rydberg orbital, only a very small barrier exists for transfer to the S–S σ^* orbital. As a result, this process is much faster and is complete within several vibrational periods [7]. Understanding this process requires accurate description of the Rydberg and valence states, as well as electronic couplings between them. Moreover, a theoretical description of this process is not complete until the coupled electron-nuclear dynamical process involving these states is characterised.

In summary, interactions between Rydberg and valence states are ubiquitous in chemistry and exemplify more general phenomena. The combined efforts of state-of-the-art experimental and theoretical techniques allows an understanding of the rich

and fascinating chemical transformations that involve multiple interacting states of different nature.

Acknowledegments

Notes

1. Dyson orbitals allow one to visualise differences between correlated multi- configurational wave functions of the neutral species and the respective cations, and are particularly useful when analysing electron distributions in excited states.
2. Note that, despite the mixed character of the interacting states, which would ordinarily be thought of as representing a multi-reference (MR) situation, their wave functions are of singly excited character, i.e. all the leading configurations appear at single excitations from the reference Φ_0. Thus, EOM-CC describes these states with the same accuracy as pure Rydberg or valence states, and is capable of correctly reproducing the degree of the mixing, provided, of course, that an appropriate one-electron basis set is employed. Reproducing this type of interaction within the MR formalism would require careful crafting of the active space at the MCSCF level and subsequent inclusion of dynamical correlation. The popular TD-DFT/ B3LYP method would fail due to self-interaction error that spoils the description of Rydberg (and charge transfer) states.
3. In doublet radicals, the states that involve excitations of 'core' electrons are problematic for single reference methods (including EOM-EE) employing a doublet reference, because they have partially doubly-excited character. These states can be better described by using EOM-SF and a quartet reference, as done in Ref. [12].

References

[1] R. F. Stebbings and F. B. Dunning, editors, *Rydberg States of Atoms and Molecules* (Cambridge University Press, Cambridge, 1983).
[2] M. B. Robin, *Higher Excited States of Polyatomic Molecules*, Vol. 1–3 (Academic Press, Inc., New York, NY, 1975).
[3] C. Sándorfy, editor, *The Role of Rydberg States in Spectroscopy and Photochemistry: Low and High Rydberg States* (Kluwer Academic Publishers, Netherlands, 1999).
[4] C. Sándorfy, Int. J. Quant. Chem. **19**, 1147 (1981); Top. Curr. Chem. **86**, 91 (1979).
[5] J. S. Zhang, in *Modern Trends in Chemical Reaction Dynamics Part II*, edited by X. Yang and L. Liu, (World Scientific, Singapore, 2004), Vol. 14 of *Advanced Series in Physical Chemistry*, pp. 465–521. and references therein.
[6] L. Salem, Science **191**, 822 (1976).
[7] M. Sobczyk and J. Simons, J. Phys. Chem. B **110**, 7519 (2006).

[8] O. Gessner, A. M. D. Lee, J. P. Shaffer, H. Reisler, S. Levchenko, A. Krylov, J. G. Underwood, H. Shi, A. L. L. East, D. M. Wardlaw, E.t-H. Chrysostom, C. C. Hayden, and A. Stolow, Science **311**, 219 (2006).

[9] T. F. Gallagher, *Rydberg Atoms* (Cambridge Monographs on Atomic, Molecular and Chemical Physics, Cambridge, 1994).

[10] G. Herzberg, *Molecular Spectroscopy and Molecular Structure; Electronic Spectra and Electronic Structure of Polyatomic Molecules*, Vol. III (van Nostrand Reinhold, New York, NY, 1966).

[11] E. O. Bernstein, D. Taylor, and C. Dion, J. Chem. Phys. **106**, 3512 (1997).

[12] L. Koziol, S. V. Levchenko, and A. I. Krylov, J. Phys. Chem. A **110**, 2746 (2006).

[13] M. Oana and A. I. Krylov, J. Chem. Phys. **127**, 234106 (2007).

[14] M. Sablier and T. Fujii, Chem. Rev. **102**, 2856 (2002).

[15] N. Muller and R. S. Mulliken, J. Am. Chem. Soc. **80**, 3489 (1958).

[16] R. Hoffman, L. Radom, J. A. Pople, P. von R. Schleyer, W. J. Here, and L. Salem, J. Am. Chem. Soc. **94**, 6221 (1972).

[17] W. R. Schneider, B. I. Nance, and T. J. Wallington, J. Am. Chem. Soc. **117**, 478 (1995).

[18] T. Häber, A. C. Blair, and D. J. Nesbitt, J. Chem. Phys. **124**, 054316 (2006).

[19] B. Karpichev, H. Reisler, A. I. Krylov, and K. Diri, J. Phys. Chem. A **112**, 9965 (2008).

[20] E. N. Sharp, P. Rupper, and T. A. Miller, Phys. Chem. Chem. Phys. **10**, 3955 (2008).

[21] S. V. Levchenko and A. I. Krylov, J. Chem. Phys. **115**, 7485 (2001).

[22] L. Feng, A. V. Demyanenko, and H. Reisler, J. Chem. Phys. **118**, 9623 (2003).

[23] L. Feng, A. V. Demyanenko, and H. Reisler, J. Chem. Phys. **120**, 6524 (2004).

[24] B. C. Hoffman and D. R. Yarkony, J. Chem. Phys. **116**, 8300 (2002).

[25] D. R. Yarkony, J. Chem. Phys. **122**, 084316 (2005).

[26] S. V. Levchenko, A. V. Demyanenko, V. Dribinski, A. B. Potter, A. I. Krylov, and H. Reisler, J. Chem. Phys. **118**, 9233 (2003).

[27] B. J. Finlayson-Pitts and J. N. Pitts, *Chemistry of the Upper and Lower Atmosphere: Theory, Experiments, and Applications* (Academic Press, New York, NY, 1999).

[28] R. Schinke, *Photodissociation Dynamics* (Cambridge Monographs on Atomic, Molecular, and Chemical Physics, Cambridge University Press, Cambridge, 1993).

[29] T. Baer and W. L. Hase, *Unimolecular Reaction Dynamics: Theory and Experiment* (Oxford University Press, New York, NY, 1996).

[30] A. Stolow, A. E. Bragg, and D. M. Neumark, Chem. Rev. **104**, 1719 (2004).

[31] L. J. Butler, Annu. Rev. Phys. Chem. **49**, 125 (1998).

[32] W. D. Domcke, D. R. Yarkony, and H. Köppel, editors, *Conical Intersections. Electronic Structure, Dynamics and Spectroscopy* (World Scientific Publ Co Pte Ltd, Singapore, 2004).

[33] G. A. Worth and L. S. Cederbaum, Annu. Rev. Phys. Chem. **55**, 127 (2004).

[34] S. T. Pratt, Rep. Prog. Phys. **58**, 821 (1995).

[35] S. T. Pratt, Rad. Phys. Chem. **70**, 435 (2004).

[36] S. T. Pratt, Annu. Rev. Phys. Chem. **56**, 281 (2005).

[37] A. G. Suits and R. E. Continetti, editors, *Imaging in Chemical Dynamics*, Vol. 770 (ACS Symposium Series, American Chemical Society, Washington, DC, 2001).

[38] B. J. Whittaker, *Imaging in Molecular Dynamics: Technology and Applications* (Cambridge University Press, Cambridge, 2003).

[39] D. Townsend, M. P. Minitti, and A. G. Suits, Rev. Sci. Inst. **74**, 2530 (2003).

[40] W. Li, S. D. Chambreau, S. A. Lahankar, and A. G. Suits, Rev. Sci. Inst. **76**, 63106 (2005).

[41] J. F. Stanton, J. Chem. Phys. **115**, 10382 (2001).

[42] N. J. Russ, T. D. Crawford, and G. S. Tschumper, J. Chem. Phys. **120**, 7298 (2004).

[43] L. V. Slipchenko and A. I. Krylov, J. Phys. Chem. A **110**, 291 (2006).

[44] T. Kowalczyk and A. I. Krylov, J. Phys. Chem. A **111**, 8271 (2007).

[45] J. F. Stanton, J. Chem. Phys. **126**, 134309 (2007).

[46] V. Vanovschi, A. I. Krylov, and P. G. Wenthold, Theor. Chim. Acta **120**, 45 (2008).

[47] D. J. Rowe, Rev. Mod. Phys. **40**, 153 (1968).
[48] K. Emrich, Nucl. Phys. **A 351**, 379 (1981).
[49] H. Sekino and R. J. Bartlett, Int. J. Quant. Chem. Symp. **26**, 255 (1984).
[50] J. F. Stanton and R. J. Bartlett, J. Chem. Phys. **98**, 7029 (1993).
[51] R. J. Bartlett and J. F. Stanton, Rev. Comp. Chem. **5**, 65 (1994).
[52] S. V. Levchenko and A. I. Krylov, J. Chem. Phys. **120**, 175 (2004).
[53] A. I. Krylov, Annu. Rev. Phys. Chem. **59**, 433 (2008).
[54] (a) K. Hirao, editor, *Recent Advances in Multi-reference Methods* (World Scientific, Singapore, 1999); (b) M. W. Schmidt and M. S. Gordon, Ann. Rev. Phys. Chem. **49**, 233, 1998.
[55] G. J. Atchity, S. S. Xantheas, and K. Ruedenberg, J. Chem. Phys. **95**, 1862 (1991).
[56] D. R. Yarkony, Rev. Mod. Phys. **68**, 985 (1996).
[57] D. R. Yarkony, Acc. Chem. Res. **31**, 511 (1998).
[58] D. R. Yarkony, J. Phys. Chem. A **105**, 6277 (2001).
[59] M. Ben-Nun and T. J. Martínez, Chem. Phys. **259**, 237 (2000).
[60] P. W. Kash, G. C. G. Waschewsky, and L. J. Butler, J. Chem. Phys. **99**, 4479 (1993).
[61] J. F. Stanton, K. W. Sattelmeyer, J. Gauss, M. Allan, T. Skalicky, and T. Bally, J. Chem. Phys. **115**, 1 (2001).
[62] M. Wladyslawski and M. Nooijen, *Low-Lying Potential Energy Surfaces, ACS Symposium Series*, Vol. 828 (ACS, Washington, DC, 2002), pp. 65–92.
[63] A. Hazra, H. H. Chang, and M. Nooijen, J. Chem. Phys. **121**, 2125 (2004).
[64] A. Hazra and M. Nooijen, J. Chem. Phys. **122**, 204327 (2005).
[65] E. Epifanovsky and A. I. Krylov, Mol. Phys. **105**, 2515 (2007).
[66] P. A. Pieniazek, S. A. Arnstein, S. E. Bradforth, A. I. Krylov, and C. D. Sherrill, J. Chem. Phys. **127**, 164110 (2007).
[67] V. A. Mozhayskiy, J. D. Savee, J. E. Mann, R. E. Continetti, and A. I. Krylov, J. Phys. Chem. A **112**, 12345 (2008).
[68] J. D. Savee, V. A. Mozhayskiy, J. E. Mann, A. I. Krylov, and R. E. Continetti, Science **321**, 826 (2008).
[69] J. Olsen, J. Chem. Phys. **113**, 7140 (2000).
[70] J. F. Stanton, J. Chem. Phys. **99**, 8840 (1993).
[71] J. F. Stanton and J. Gauss, J. Chem. Phys. **101**, 8938 (1994).
[72] S. V. Levchenko, T. Wang, and A. I. Krylov, J. Chem. Phys. **122**, 224106 (2005).
[73] P. A. Pieniazek, S. E. Bradforth, and A. I. Krylov, J. Chem. Phys. **129**, 074104 (2008).
[74] A. I. Krylov, Acc. Chem. Res. **39**, 83 (2006).
[75] H. Koch, H. J.Aa. Jensen, P. Jørgensen, and T. Helgaker, J. Chem. Phys. **93**, 3345 (1990).
[76] M. Nooijen and R. J. Bartlett, J. Chem. Phys. **102**, 3629 (1995).
[77] D. Sinha, D. Mukhopadhya, R. Chaudhuri, and D. Mukherjee, Chem. Phys. Lett. **154**, 544 (1989).
[78] A. I. Krylov, Chem. Phys. Lett. **338**, 375 (2001).
[79] J. F. Stanton and J. Gauss, Adv. Chem. Phys. **125**, 101 (2003).
[80] H. Larsen, K. Hald, J. Olsen, and P. Jørgensen, J. Chem. Phys. **115**, 3015 (2001).
[81] P. G. Szalay and J. Gauss, J. Chem. Phys. **112**, 4027 (2000).
[82] D. Maurice and M. Head-Gordon, Int. J. Quant. Chem. Symp. **29**, 361 (1995).
[83] Y. Shao, L. F. Molnar, Y. Jung, J. Kussmann, C. Ochsenfeld, S. Brown, A. T. B. Gilbert, L. V. Slipchenko, S. V. Levchenko, D. P. O'Neil, R. A. Distasio Jr, R. C. Lochan, T. Wang, G. J. O. Beran, N. A. Besley, J. M. Herbert, C. Y. Lin, T. Van Voorhis, S. H. Chien, A. Sodt, R. P. Steele, V. A. Rassolov, P. Maslen, P. P. Korambath, R. D. Adamson, B. Austin, J. Baker, E. F. C. Bird, H. Daschel, R. J. Doerksen, A. Drew, B. D. Dunietz, A. D. Dutoi, T. R. Furlani, S. R. Gwaltney, A. Heyden, S. Hirata, C.-P. Hsu, G. S. Kedziora, R. Z. Khalliulin, P. Klunziger, A. M. Lee, W. Z. Liang, I. Lotan, N. Nair, B. Peters, E. I. Proynov, P. A. Pieniazek, Y. M. Rhee, J. Ritchie, E. Rosta, C. D. Sherrill, A. C. Simmonett,

J. E. Subotnik, H. L. Woodcock III, W. Zhang, A. T. Bell, A. K. Chakraborty, D. M. Chipman, F. J. Keil, A. Warshel, W. J. Herhe, H. F. Schaefer III, J. Kong, A. I. Krylov, P. M. W. Gill, and M. Head-Gordon, Phys. Chem. Chem. Phys. **8**, 3172 (2006).

[84] J. F. Stanton, J. Gauss, J. D. Watts, W. J. Lauderdale, and R. J. Bartlett, ACES II, 1993. The package also contains modified versions of the MOLECULE Gaussian integral program of J. Almlöf and P.R. Taylor, the ABACUS integral derivative program written by T.U. Helgaker, H.J.Aa. Jensen, P. Jørgensen and P.R. Taylor, and the PROPS property evaluation integral code of P.R. Taylor.

[85] A. Stolow, Annu. Rev. Phys. Chem. **54**, 89 (2003).

[86] A. J. R. Heck and D. W. Chandler, Annu. Rev. Phys. Chem. **46**, 335 (1995).

[87] D. H. Parker and A. Eppink, Rev. Sci. Instr. **68**, 3477 (1997).

[88] M. N. R. Ashfold, N. H. Nahler, A. J. Orr-Ewing, O. P. J. Vieuxmaire, and R. L. Toomes, Phys. Chem. Chem. Phys. **8**, 26 (2006).

[89] H. Offerhaus, C. Nicole, F. Lepine, C. Bordas, F. Rosca-Pruna, and M. Vrakking, Rev. Sci. Instr. **72**, 3245 (2001).

[90] E. Wrede, S. Laubach, S. Schulenburg, A. Brown, E. Wouters, A. J. Orr-Ewing, and M. N. R. Ashfold, J. Chem. Phys. **114**, 2629 (2001).

[91] V. Dribinski, A. Ossadtchi, V. A. Mandelshtam, and H. Reisler, Rev. Sci. Instrum. **73**, 2634 (2002).

[92] J. A. Syage, J. Chem. Phys. **105**, 1007 (1996).

[93] J. H. Wang, Y. T. Su, and K. Liu, J. Phys. Chem. **101**, 6593 (1997).

[94] L. Schnieder, W. Meier, K. H. Welge, M. N. R. Ashfold, and C. M. Western, J. Chem. Phys. **92**, 7027 (1990).

[95] M. N. R. Ashfold, I. R. Lambert, D. H. Mordaunt, G. P. Morley, and C. M. Western, J. Phys. Chem. **96**, 2938 (1992).

[96] W. D. Zhou, Y. Yuan, and J. S. Zhang, J. Chem. Phys. **119**, 9989 (2003).

[97] G. Amaral, K. S. Xu, and J. S. Zhang, J. Chem. Phys. **114**, 5164 (2001).

[98] F. Raulin, M. Khlifi, M. Dang-Nhu, and D. Gautier, Adv. Space. Res. **12**, 181 (1992).

[99] F. W. Kirkbride and R. G. Norrish, J. Chem. Soc. **136**, 119 (1933).

[100] I. Fedorov, L. Koziol, G. Li, J. A. Parr, A. I. Krylov, and H. Reisler, J. Phys. Chem. A **111**, 4557 (2007).

[101] L. Koziol, I. Fedorov, G. Li, J. A. Parr, H. Reisler, and A. I. Krylov, J. Phys. Chem. A **111**, 13347 (2007).

[102] A. J. Merer, Can. J. Phys. **42**, 1242 (1964).

[103] C. B. Moore, J. Chem. Phys. **39**, 1884 (1963).

[104] C. B. Moore and G. C. Pimentel, J. Chem. Phys. **40**, 329 (1964).

[105] J. Bastide and J. P. Maier, Chem. Phys. **12**, 177 (1976).

[106] S. P. Walch and W. A. Goddard III, J. Am. Chem. Soc. **97**, 5319 (1975).

[107] M. Rittby, S. Pal, and R. J. Bartlett, J. Chem. Phys. **90**, 3214 (1989).

[108] O. Shimamura, *Topics in Stereochemistry* (Wiley, New York, NY, 1969).

[109] H. Okabe, *Photochemistry of Small Molecules* (Wiley, New York, NY, 1978).

[110] W. C. Gardiner, editor, *Gas-Phase Combustion Chemistry* (Springer, New York, NY, 2000).

[111] L. Fensterbank, M. Malacria, and S. M. Sieburth, Synthesis **8**, 813 (1997).

[112] V. Dribinski, A. V. Demyanenko, A. B. Potter, and H. Reisler, J. Chem. Phys. **115**, 7474 (2001).

[113] L. Andrews and D. W. Smith, J. Chem. Phys. **53**, 2956 (1970).

[114] J. Verges, C. Effantin, J. d'Incan, D. L. Cooper, and R. F. Barrow, Phys. Rev. Lett. **53**, 46 (1984).

[115] Ch. Meier and V. Engel, Chem. Phys. Lett. **212**, 691 (1993).

[116] Ch. Meier and V. Engel, J. Chem. Phys. **101**, 2673 (1994).

[117] Y. Arasaki, K. Takatsuka, K. Wang, and V. McKoy, J. Chem. Phys. **112**, 8871 (2000).

[118] M. S. Gordon and J. W. Caldwell, in *Excited States in Organic Chemistry and Biochemistry*edited by B. Pullman and N. Goldblum (D. Reidel publishing company, Dordrecht, Holland, 1977), pp. 257–270.

[119] E. D. Glendening, J. K. Badenhoop, A. E. Reed, J. E. Carpenter, J. A. Bohmann, C. M. Morales, and F. Weinhold, NBO 5.0 (Theoretical Chemistry Institute, University of Wisconsin, Madison, WI, 2001).

[120] I. Martín, A. M. Velasco, and C. Lavín, Int. J. Quant. Chem. **86**, 59 (2002).

[121] L. Feng, X. Huang, and H. Reisler, J. Chem. Phys. **117**, 4820 (2002).

[122] J. Wei, B. Karpichev, L. W. Edwards, and H. Reisler, J. Phys. Chem. A **112**, 412 (2008).

[123] J. W. Hudgens, C. S. Dulcey, G. R. Long, and D. J. Bogan, J. Chem. Phys. **87**, 4546 (1987).

[124] J. W. Hudgens, T. G. DiGiuseppe, and M. C. Lin, J. Chem. Phys. **79**, 571 (1983).

[125] J. Munk, P. Pagsberg, E. Ratajczak, and A. Sillesen, J. Phys. Chem. **90**, 2752 (1986).

[126] R. D. Johnson III and J. F. Hudgens, J. Phys. Chem. **100**, 19874 (1996).

[127] V. Aristov, D. Conroy, and H. Reisler, Chem. Phys. Lett. **318**, 393 (2000).

[128] D. Conroy, V. Aristov, L. Feng, and H. Reisler, J. Phys. Chem. **104**, 10288 (2000).

[129] P. J. Bruna and F. Grein, J. Phys. Chem. A **102**, 3141 (1998).

[130] P. J. Bruna and F. Grein, J. Phys. Chem. A **105**, 8599 (2001).

[131] G. Herzberg, Proc. Ro. Woc. London Ser. A **262**, 291 (1961).

[132] S. Matsika and D. R. Yarkony, J. Am. Chem. Soc. **125**, 10672 (2003).

[133] S. Matsika and D. R. Yarkony, J. Chem. Phys. **117**, 6097 (2002).

[134] L. Feng and H. Reisler, J. Phys. Chem. A **108**, 9847 (2004).

[135] P. A. Cleary, M. T. B. Romero, M. A. Blitz, D. E. Heard, M. J. Pilling, P. W. Seakins, and L. Wang, Phys. Chem. Chem. Phys. **8**, 5633 (2006).

[136] K. Hoyermann, M. Olzmann, J. Seeba, and B. Viskolcz, J. Phys. Chem. A **103**, 5692 (1999).

[137] J. Lindner, R. A. Loomis, J. J. Klaassen, and S. R. Leone, J. Chem. Phys. **108**, 1944 (1998).

[138] J. P. Senosiain, S. J. Klippenstein, and J. A. Miller, J. Phys. Chem. A **110**, 6960 (2006).

[139] F. P. Tully, Chem. Phys. Lett. **143**, 510 (1988).

[140] C. A. Taatjes, N. Hansen, A. McIlroy, J. A. Miller, J. P. Senosiain, S. J. Klippenstein, F. Qi, L. S. Sheng, Y. W. Zhang, T. A. Cool, J. Wang, P. R. Westmoreland, M. E. Law, T. Kasper, and K. Kohse-Hoinghaus, Science **308**, 1887 (2005).

[141] B. Ruscic and J. Berkowitz, J. Chem. Phys. **101**, 10936 (1994).

[142] J. M. Dyke, A. R. Ellis, N. Jonathan, N. Keddar, and A. Morris, Chem. Phys. Lett. **111**, 207 (1984).

[143] J. M. Dyke, P. Groves, E. P. F. Lee, and M. H. Z. J. Niavaran, J. Phys. Chem. A **101**, 373 (1997).

[144] T. L. Gilbert, I. Grebner, I. Fischer, and P. Chen, J. Chem. Phys. **110**, 5485 (1999).

[145] Z. Min, R. Quandt, and R. Bersohn, Chem. Phys. Lett. **296**, 372 (1998).

[146] J. L. Brum, S. Deshmukh, and B. Koplitz, J. Chem. Phys. **95**, 2200 (1991).

[147] J. L. Brum, S. Deshmukh, and B. Koplitz, J. Chem. Phys. **98**, 1178 (1990).

[148] R. Quandt, X. Wang, Z. Min, H. L. Kim, and R. Bersohn, J. Phys. Chem. A **102**, 6063 (1998).

[149] G. W. Johnston, S. Satyapal, R. Bersohn, and B. Katz, J. Chem. Phys. **92**, 206 (1990).

[150] B. Noller and I. Fischer, J. Chem. Phys. **126**, 144302 (2007).

[151] M. Zierhut, W. Roth, and I. Fischer, J. Phys. Chem. A **108**, 8125 (2004).

[152] A. Sevin, H. T. Yu, and E. M. Evleth, J. Mol. Struct.: THEOCHEM **104**, 163 (1983).

[153] E. M. Evleth, H. Z. Cao, E. Kassab, and A. Sevin, Chem. Phys. Lett. **109**, 45 (1984).

[154] A. S. Zyubin, A. M. Mebel, and S. H. Lin, Chem. Phys. Lett. **323**, 44 (2000).

[155] A. Bach, J. M. Hostettler, and P. Chen, J. Chem. Phys. **123**, 021101 (2005).

[156] A. Bach, J. M. Hostettler, and P. Chen, J. Chem. Phys. **125**, 024304 (2006).

[157] J. M. Hostettler, A. Bach, and P. Chen, J. Chem. Phys. **130**, 034303 (2009).

[158] J. C. Tully, J. Chem. Phys. **93**, 1061 (1990).

[159] J. A. Davies, J. E. LeClaire, R. E. Continetti, and C. C. Hayden, J. Chem. Phys. **111**, 1 (1999).

[160] J. A. Davies, R. E. Continetti, D. W. Chandler, and C. C. Hayden, Phys. Rev. Lett. **84**, 5983 (2000).
[161] I. Fischer and P. Chen, J. Phys. Chem. A **106**, 4291 (2002).
[162] I. Fischer, Int. J. Mass Spectr. **216**, 131 (2002).
[163] B. Noller, R. Maksimenka, I. Fischer, M. Armone, B. Engels, C. Alcaraz, L. Poisson, and J. M. Mestdagh, J. Phys. Chem. A **111**, 1771 (2007).
[164] E. S. Whitney, T. Haeber, M. D. Schuder, A. C. Blair, and D. J. Nesbitt, J. Chem. Phys. **125**, 54303 (2006).
[165] K. Piechowska-Strumik, D. Lauvergnat, M. C. Bacchus-Montabonel, and M. Desouter-Lecomte, Chem. Phys. Lett. **425**, 16 (2006).
[166] K. Piechowska-Strumik, M. C. Bacchus-Montabonel, Y. S. Tergiman, and J. E. Sienkiewicz, Chem. Phys. Lett. **425**, 225 (2006).
[167] L. R. McCunn, B. L. FitzPatrick, M. J. Krisch, L. J. Butler, C. W. Liang, C. W, and J. J. Lin, J. Chem. Phys. **125**, 33306 (2006).
[168] H. Fan and S. T. Pratt, J. Chem. Phys. **124**, 44313 (2006).
[169] H. Fan and S. T. Pratt, J. Chem. Phys. **125**, 44302 (2006).
[170] R. A. Young and D. R. Yarkony, J. Chem. Phys. **123**, 84315 (2005).
[171] N. E. Sveum, S. J. Goncher, and D. M. Neumark, Phys. Chem. Chem. Phys. **8**, 592 (2005).
[172] L. McCunn, M. J. Krisch, Y. Liu, L. J. Butler, and J. N. Shu, J. Phys. Chem. A **109**, 6430 (2005).
[173] A. E. Faulhaber, D. E. Szpunar, K. E. Kautzman, and D. M. Neumark, J. Phys. Chem. A **109**, 10239 (2005).
[174] H. Y. Fan and S. T. Pratt, J. Chem. Phys. **123**, 4301 (2005).
[175] M. H. Kim, L. Shen, H. Tao, T. J. Martinez, and A. G. Suits, Science **315**, 1561 (2007).
[176] H. Reisler, Ann. Rev. Phys. Chem. **60**, 39 (2009).
[177] A. M. Virshup, C. Punwong, T. V. Pogorelov, B. Lindquist, C. Ko, and T. J. Martinez, J. Chem. Phys. (2009), inpress.
[178] A. Toniolo, B. Levine, A. Thompson, J. Quenneville, M. Ben-Nun. J. Owens, S. Olsen, L. Manohar, and T. J. Martinez, in *Computational Methods in Organic Photochemistry*, edited by A. Kutateladze (Marcel-Dekker, New York, NY, 2005).
[179] A. Sawicka, P. Skurski, R. R. Hudgins, and J. Simons, J. Phys. Chem. B **107**, 13505 (2003).